LRP 768/03 August 2003

Papers presented at the IAEA Technical Meeting on ECRH Physics and Technology for ITER

Kloster Seeon, Germany, July 2003

Available in colour on the web at
http://crppwww/conferences/

ISSN 0458-5895

LIST OF CONTENTS

ECRH and ECCD Physics in the TCV Tokamak

S. Alberti, G. Arnoux, P. Blanchard, Y. Camenen, S. Coda, T.P. Goodman, M. Henderson, J.P. Hogge, J.-M. Moret, E. Nelson-Melby, P. Nikkola, A. Pochelon, L. Porte, O. Sauter, M.Q. Tran, and TCV Team

Centre de Recherches en Physique des Plasmas,
Association EURATOM-Confédération Suisse,
EPFL, 1015 Lausanne, Switzerland

Introduction

The main advantage of an ECH system is its ability to heat and drive current in a magnetized plasma, locally. In a next step Tokamak like ITER this is essential for controlling confinement degrading localized MHD instabilites such as the Neoclassical Tearing Modes (NTM) or the sawtooth instability near the q=1 rational surface. The ECH system installed on the TCV Tokamak, with a total of 4.1MW of injected power, with a highly flexible launching mirror system that allows real-time control of the toroidal and poloidal mirror angles, is, at present, one of the most relevant ECH systems for ITER. A variety of tools are used for modeling the localized electron heating and current drive. These include: a ray-tracing code for calculating the wave propagation, a relativistic model for the polarization and power absorption and a Fokker-Planck model including spatial diffusion for the ECCD current drive calculation.

With the TCV ECH system, in addition to a scientific program based on applications of ECRH/ECCD to confinement and MHD stability, an extensive effort has been devoted to validating the different models in terms of the localization properties. In this paper, the experimental methods used to determine the absorption profiles for the power and driven current are presented. The stabilisation of local MHD instabilities requires, first, a high aiming accuracy on the launcher system and, second, the ability to follow an eventual radial movement of these instabilities. Real-time feedback on the power deposition radius needs to be implemented. Both, accuracy and real-time control are adressed in this paper: the characteristic aiming accuracy of the very sensitive X3 launching scheme is presented and, in relation to the real-time feedback, some possible limitations on the real-time determination of the deposition radius are discussed.

The TCV ECRH-ECCD system

The ECRH-ECCD system has recently been completed and is composed by 9 gyrotrons (Figure 1) divided in three clusters. Each cluster is connected to a single high voltage power supply. Two of the clusters each have 3 gyrotrons (82.7GHz, 0.5MW, 2s) used for heating (ECH) and/or current-drive generation (ECCD) in 2nd harmonic X-mode (X2)[1] while the third cluster has 3 gyrotrons (118GHz, 0.5MW, 2s) for top-launch third harmonic X-mode (X3) heating[2]. At the toroidal magnetic field of 1.5T, the X-mode cut-off densities for the X2 and X3 waves are 4.2 10^{19}[m^{-3}] and 11.5$10^{19}$[m^{-3}], respectively.

The X2(X3) gyrotron rf output, is connected to an rf conditioning unit (RFCU) whose optics is composed by 4(3) mirrors. There are two(one) parabolic mirrors for adapting the rf beam to the HE_{11} waveguide and two flat gratings for controlling the wave polarization.

For a given plasma equilibrium and a predefined launching angle, for the X2 gyrotrons, the required polarizer angles are calculated and than physically set to these calculated values using a motorized system. Each RFCU is connected to a 63.5mm evacuated HE_{11} waveguide. For the X2 gyrotrons each line is connected to a low-field side launcher which has two angular degrees of freedom. One degree of freedom has real-time steering capability with a maximum angular sweep rate of 48 °/sec (96°/sec for the rf beam). The mirror orientation can be such as to either sweep, during the plasma shot, the poloidal or the toroidal injection angles (Figure 2). The waveguides from the X3 gyrotrons converge to a single top-launch mirror which has radial and poloidal angle degrees of freedom. The X3 mirror angle has a real-time steering capability of 20°/sec (40°/sec for the rf beam) while the radial position can be changed between shots.

With the very flexible position and shape control capability of theTCV plasmas, the real-time steering capabilities of the launching angles both for the X2 and X3 have proven to be essential. For a given target plasma, the real time steering of the rf beams primarly permits experiments to be performed that would be significantly more difficult to analyse and interpret if performed on a shot to shot basis but also opens the door to the implementation of a feedback system to control in real-time the power deposition location and/or driven current.

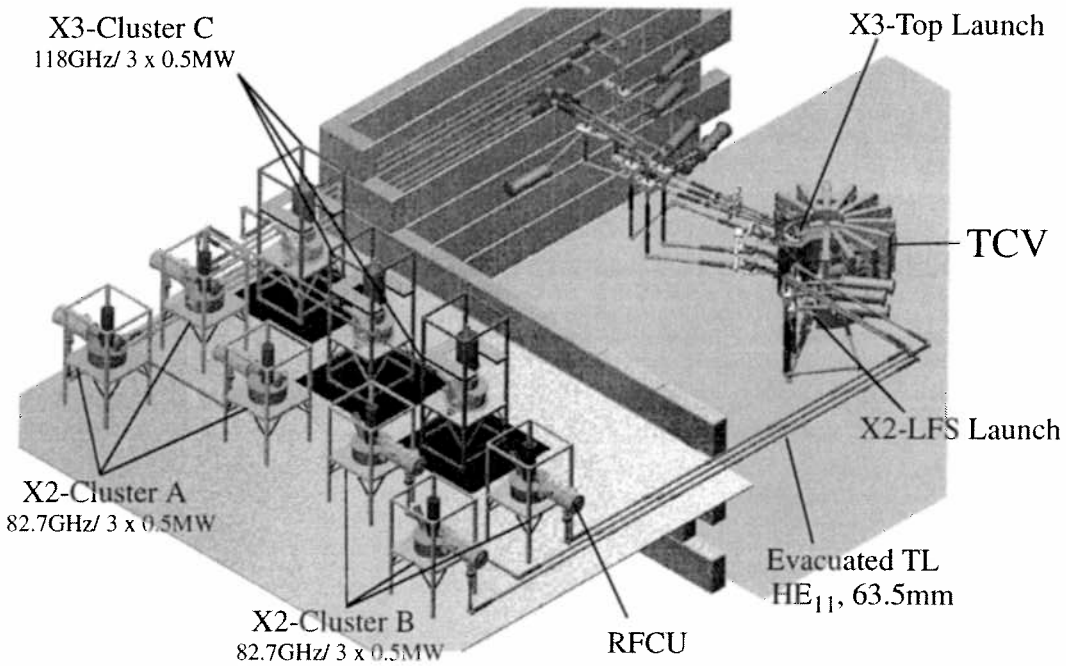

Figure 1. The TCV ECRH system. Three clusters of gyrotrons, A (X2, 82.7GHz 3x0.5MW), B (X2, 82.7GHz 3x0.5MW), C (X3,118GHz 3x0.5MW). Each cluster is connected to one High Voltage power supply (V_b = 85kV, I_b=80A, T_{max} = 2s). At each gyrotron rf output, a rf Conditioning Unit (RFCU) contains an for efficiently couple the rf beam into the HE_{11} (63.55mm diameter) waveguide as well as control the rf beam polarization..

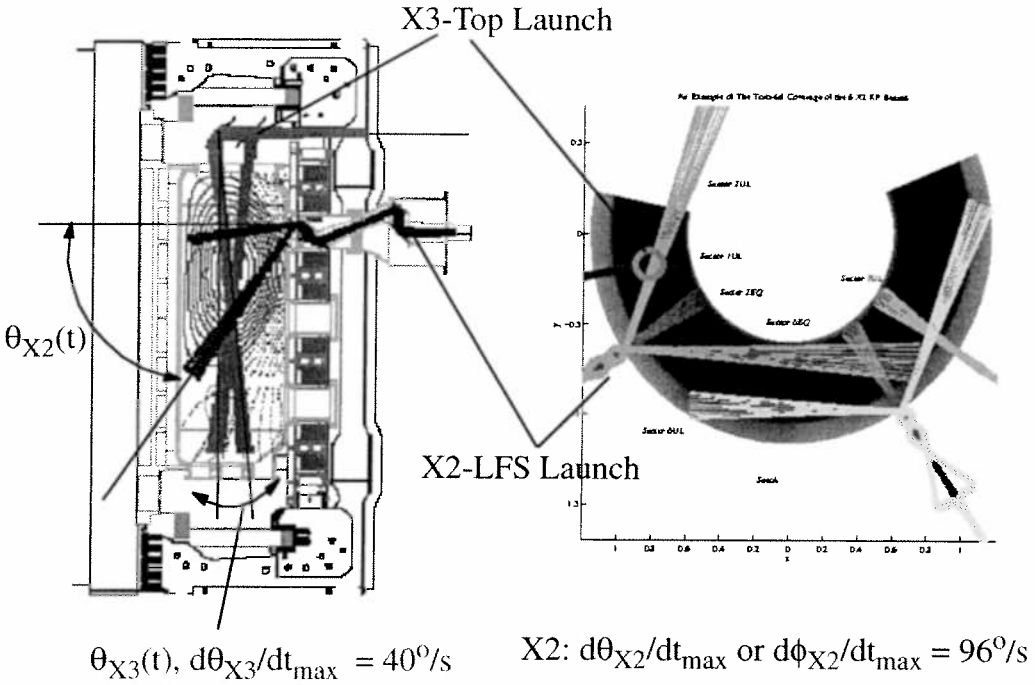

Figure 2. Real-time steering capabilities of the X2 and X3 launchers.

Figure of merit of an ECH-ECCD system

The highly efficient and localized heating and current drive capabilities of ECH-ECCD in magnetic fusion devices are based on a resonant wave particle interaction which takes place both in real and phase space. The localization properties can essentially be described by a gaussian function: $A(\rho) = A_0 \, Exp[-(\rho-\rho_0)^2/\Delta\rho^2]$, where the quantity, A, represents a relevant physical quantity such as the power density dP/dV [MW/m^3] and/or driven current j_{ECCD} [MA/m^2]. The localization properties are described by the deposition radius, ρ_0, and the width $\Delta\rho$. For a given plasma configuration and ECH system, the three quantities, $(A_0,\rho_0,\Delta\rho)$ depend essentially on: the installed power, the rf beam optics and aiming accuracy, refraction effects, and diffusion processes both in real and phase space. The rf power density at a given deposition radius is approximately given by:

$$dP/dV\ (r) \quad P_{RF}/\ (8\pi^{5/2}\, r_0\, \Delta r\, \kappa\, R_0)*Exp[-(r-r_0)^2/\Delta r^2]\ [W/m^3],(r_0 > 1.5\Delta r\ )$$

where P_{RF} is the total beam power, r_0 is the deposition radius, κ is the plasma elongation, R_0 is the major radius and Δr is the deposition width. Δr can either be dominated by the beam optics ($\Delta r \quad w_{0p}$, where w_{0p} is the beam spot size in power) or by the absorption layer width, L_{abs},($\Delta r \quad L_{abs} < w_{0p}$) for high field side deposition. For the beam optics of the TCV X2 launcher (w_{0p} = 20mm), the typical power densities versus normalised deposition radius,ρ_{dep} ,are shown in figure 3, where the gaussian deposition profiles for two different power levels [1.35MW (red curve) and 0.45MW (blue curve)] are centered at, ρ_{dep} = 0.3. The power deposition profile for a total rf power of 1.35MW injected with the X3 top-launch is shown by the dashed black curve. Contrary to the case of the X2 LFS injection, the deposition

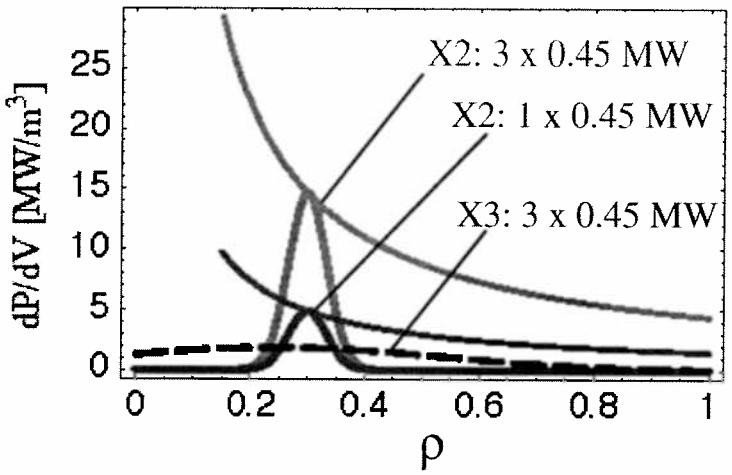

Figure3. Typical power densities for the X2 and X3 system on TCV. For the X2 system, the deposition radius is located at ρ_{dep} = 0.3 and the power deposition width is determined by the beam optics with a spot size (in power) of w_{0p} = 20mm ($\Delta\rho = w_{0p}/(\kappa a)$=0.012, a=0.25m, κ =1.7). The continuous lines passing through the peak density show how the peak density varies with deposition radius. For the X3 top launch, the deposition width is determined by both the beam optics and the ray trajectory within the resonant layer.

profile for the X3 is not local and is mainly used as a global heating in plasmas with electron densities higher than the X2 cut-off.

Models validation

The absorption profiles in TCV are calculated using the ray tracing code TORAY-GA[3] with the ray tracing part modeled by a cold plasma dispersion relation and the wave polarization and absorption calculated by a fully relativistic model assuming an isotropic, Maxwellian velocity distribution function. The plasma parameters used in TORAY-GA calculations are the bulk electron temperature and density profiles measured by Thomson scattering and the equilibrium reconstruction given by the LIUQE code[4]. In presence of a significant fraction of suprathermal electrons, in particular for the X3 wave, the absorbed fraction can be significantly underestimated by TORAY-GA and, in addition, the absorption profile can strongly deviate from the one based on a single Maxwellian distribution function[5].

Based on the ray-tracing trajectories and polarizations calculated with TORAY-GA, the current driven profile is calculated by codes based on a quasi-linear Fokker-Planck (FP) model. The fastest computational method, which is based on the Cohen[3] or Lin-Liu model for ECCD[3], is imbedded in the TORAY-GA code and gives a current driven profile, $j_{ECCD}(\rho)$, varying linearly with the power deposition profile, $dP/dV(\rho)$. Non-linear effects of the injected power are taken into account by the CQL3D code[6] which solves the FP equation in momentum space [2D, bounce average] and 1D spatial space (radial) using an rf quasilinear operator. In this model the effect of a parallel electric field can be included. As shown by Harvey et al.[6], the power dependence on the driven current deviates from its linear dependence for normalised power densities $Q = dP/dV[MW/m^3]/n_e[10^{19}m^{-3}]^2 > 0.5$. At normalised power densities Q>>0.5, as it is possible to achieve in TCV plasmas, the effect of spatial diffusion on the current carrying electrons has to be included in the CQL3D Fokker-Planck code[7,8].

Considering a flat electron density profile $n_e(\rho) = n_{e0}(1-\rho^{10})$, a comparison of the power density, $dP/dV(\rho)$, and normalised power density profiles $Q(\rho)$ between different ECH systems installed on present and future devices is shown in Figure 4. The profiles are shown for a deposition radius, $\rho_{dep} = 0.65$, which corresponds to the q=3/2 rational surface for ITER. The rf power used in the calculation is representative, for each system, of the maximum power deposited on a defined ρ_{dep}, and the beam width, used in the calculation is representative for each system.

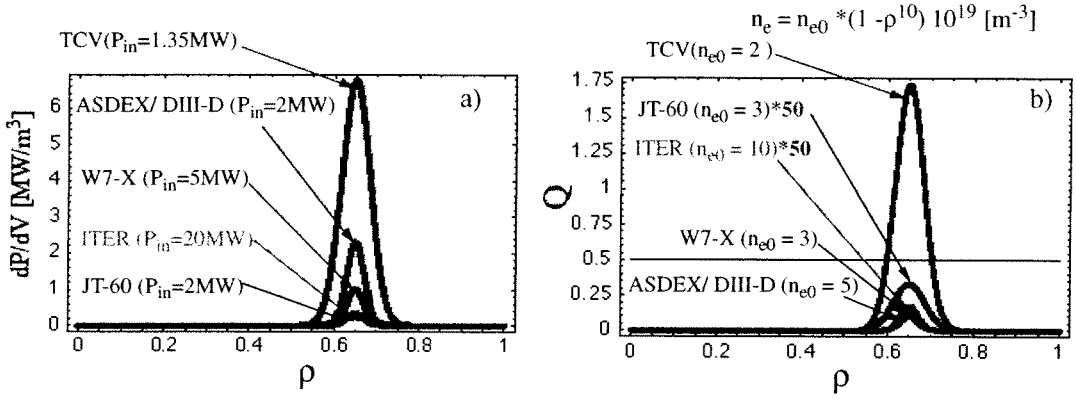

Figure4. Comparison of, a) power densities, and b) normalised power densities for different ECH systems installed on present and future tokamaks or stellerators. Notice that the normalized power density values for JT-60 and ITER have been multiplied by a factor of 50.

It is clear from this figure, that in case of ITER, non-linear effects as well as spatial diffusion effects on the current driven profile will be negligible. Extensive experimental studies of the ECCD efficiency with normalised densities Q 1, have been carried out in the DIII-D Tokamak and confirm that the linear calculation of the driven current is in good agreement with the experiment[9]. The TCV ECH system allows one to investigate both, moderate, (Q 1)[10], and high (Q 5-15) Q values. For the latter case it has been experimentally demonstrated that the current drive efficiency is dominated by spatial diffusion effects[7,8].

Experimental methods used for model validations

With the highly flexible ECH system installed on TCV, an extensive scientific program has been devoted to model validation as well as the real time control of the power deposition. These studies include, the evaluation of the aiming accuracy of the launcher mirrors and, the determination of the deposition location and width of both ECH and ECCD. In relation to the driven current, TCV has no diagnostics able to make a direct local measurement of the driven current profile, but indirect measurements using an in-situ diagnostic, such as the q=1 surface[10,11] or global measurements in fully ECCD plasma are used to determine the driven current profile.

The launcher aiming accuracy in TCV is determined by sweeping the rf beam during the plasma discharge and by either observing the sawteeth response on the q=1 surface[10], or, in the case of the X3 top launch, by measuring the global electron temperature increase during the sweep of the poloidal injection angle. For the latter launching scheme, due to the

long ray-path in the resonance layer, the aiming accuracy has to be as high as $\Delta\theta < 0.5^0$as shown in Figure 5. Both the measured optimum aiming angle and the angle width are in good agreement with the angular dependence of the absorption calculated using TORAY-GA.

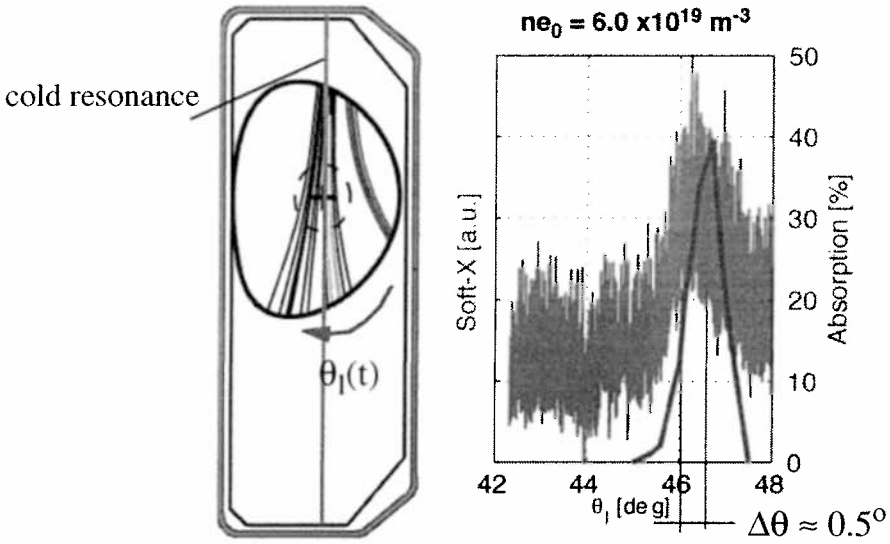

Figure 5. Comparison of the predicted absorption (TORAY-GA) versus top-launch mirror angle (θ_l) and the plasma response by a line integrated soft-X diagnostic (the electron density variation during the sweep is negligible).

A similar aiming accuracy is required for NTM stabilization in ITER using the top-launch injection. For X3 top-launch in TCV, the variation of the optimum aiming angle with plasma parameters (electron temperature, Shafranov shift, etc..) is of the same order as the aiming accuracy. In order to maintain optimal absorption a feedback system has been designed [12] and will be tested in the near future.

The experimental validation of the deposition location and deposition profile has been performed both by studying the sawtooth period response on the q=1 surface [10,11] or by modulating the injected rf power (MECH)[13]. The latter method is potentially capable of giving the deposition radius in real time, by calculating, via an FFT, the minimum phase between the drive signal and the plasma response as measured using a spatially resolved diagnostic (e.g ECE). For real time control of the deposition radius, as required for NTM stabilisation in ITER, this method could be used for generating the error signal in a feedback loop. However, in the presence of sawooth activity or ELM's, the coupling between these perturbations and the MECH signal can render the FFT method useless as shown in Figure 6 and Figure 7(left) for a case with central deposition. In figure 6(a), the time traces of the MECH are shown together with raw Soft-X signals for different lines of sight and a Fourier spectrum of the raw data (b) clearly indicates the presence of sawteeth-MECH coupling. The amplitude and phase reconstruction, using an FFT analysis, is shown in Figure 7(left) for the first three harmonics of the MECH, where amplitude (top) and phase (bottom) are shown versus normalized minor radius. The positions of the power deposition and inversion radii are respectively indicated by the green and blue vertical dashed lines. It is clear form this figure that with the FFT analysis, the minimum phase criteria does not correspond to the deposition

radius but to the inversion radius. This result is due to the strong coupling between the two dynamics associated with the sawteeth and the MECH.

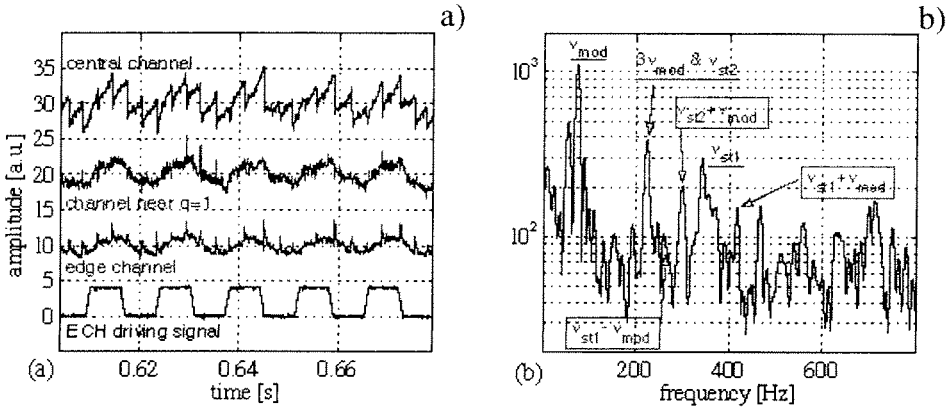

Figure 6. (a) MECH drive signal and raw Soft-X signals for different lines of sight. (b) Fourier spectrum of raw data: different peaks related to different frequencies are visible, in particular the sawtooth-modulation coupling.

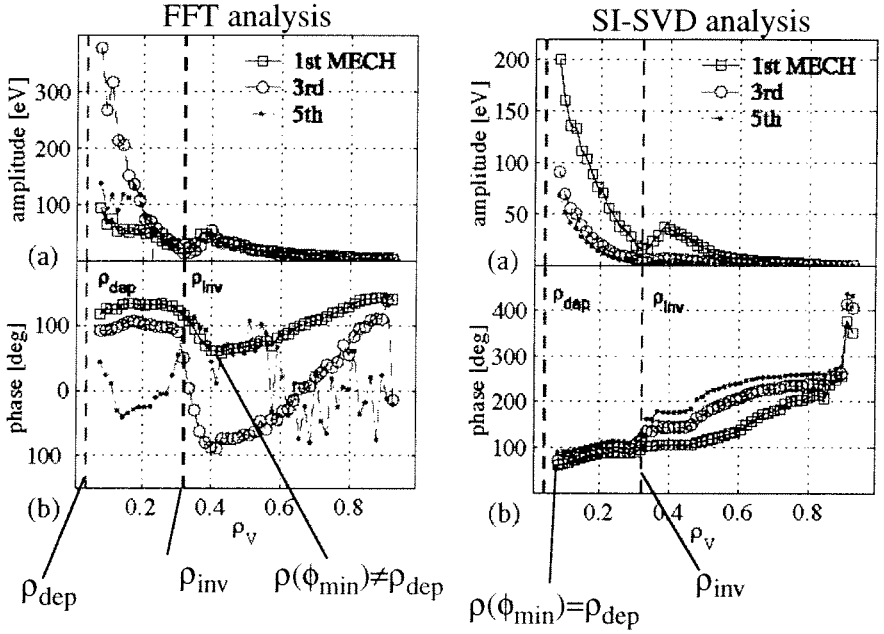

Figure 7. Left figure, amplitude(a) and phase(b) profiles at higher harmonics (first,third and fifth) of the signal treated with an FFT analysis. Right figure, amplitude(a) and phase(b) profiles at higher harmonics (first, third and fifth) of the signal treated with an SI-SVD analysis.

Several analysis methods have been investigated in order to decouple the two dynamics, and, as shown by Manini et al.[13], a new method based on system identification (SI) using a

Singular Value Decomposition (SVD), is capable of simultaneously separating the MECH form the sawtooth contribution. The result of this analysis is shown in Figure 7(right) where the power absorption radius clearly corresponds to the minimum phase criteria. In addition, the high quality of the amplitude and phase reconstructions given by the SI-SVD method makes it a powerful tool for transport analysis. In the case of off-axis ECH deposition, ($\rho_{dep} > \rho_{inv}$), the sawteeth perturbation is significantly weaker and the FFT analysis is sufficient for determining the deposition radius using the minimum phase criterion. Due to the time consuming numerical calculations involved, the SI-SVD method is not applicable for determining the power deposition radius in real-time. The SI-SVD analysis is, however, necessary for a precise amplitude and phase reconstruction needed in transport studies.

In the case of NTM stabilization in ITER[14], occuring on the rational surfaces q=3/2 ($\rho_{dep} = 0.66$) and q=2 ($\rho_{dep} = 0.79$), real-time determination of the power deposition radius via a FFT analysis might be possible provided that perturbations generated by ELM"s (and/or sawteeth), are negligible.

As mentioned earlier, the validation of the current drive profile is not possible in TCV by a direct measurement. However, it has been shown[10,11] that the sawteeth period variation is directly linked to the local current drive profile via a modification of the local shear near the q=1 surface. For experiments at low normalised power density (Q 1) using ECCD for sawtooth stabilisation[10], it has been shown that the sawteeth period variation follows the current driven profile predicted by TORAY-GA.

At large normalised power density (Q >>0.5), as typically used in TCV for fully sustained non-inductively driven ECCD discharges (Figure 8), the total experimental ECCD driven current, $I_{ECCDexp}$, is calculated by substracting from the measured plasma current, the bootstrap fraction calculated from the pressure profiles given by Thomson scattering (Figure 8(b)). Comparing the experimental value of $I_{ECCDexp}$ to the predicted value by the different models (Figure 8(c)), it is clear that radial diffusion (CQL3D+D) needs to be included in order to be consistent with the experimental observations. It is important to notice that despite the significant decrease induced by the radial diffusion on the value predicted by CQL3D, the non-linear effects are still important since the value calculated with CQL3D +D and matching the experiment is approximately a factor of 2 higher than the one predicted by the linear code TORAY-GA. The important effect of the radial diffusion is on the strong broadening of the current driven profile. For TCV power densities, CQL3D+D simulations of hard X-ray emissivity yield typically $D_0 \sim 0.5\text{-}3 m^2/s$.

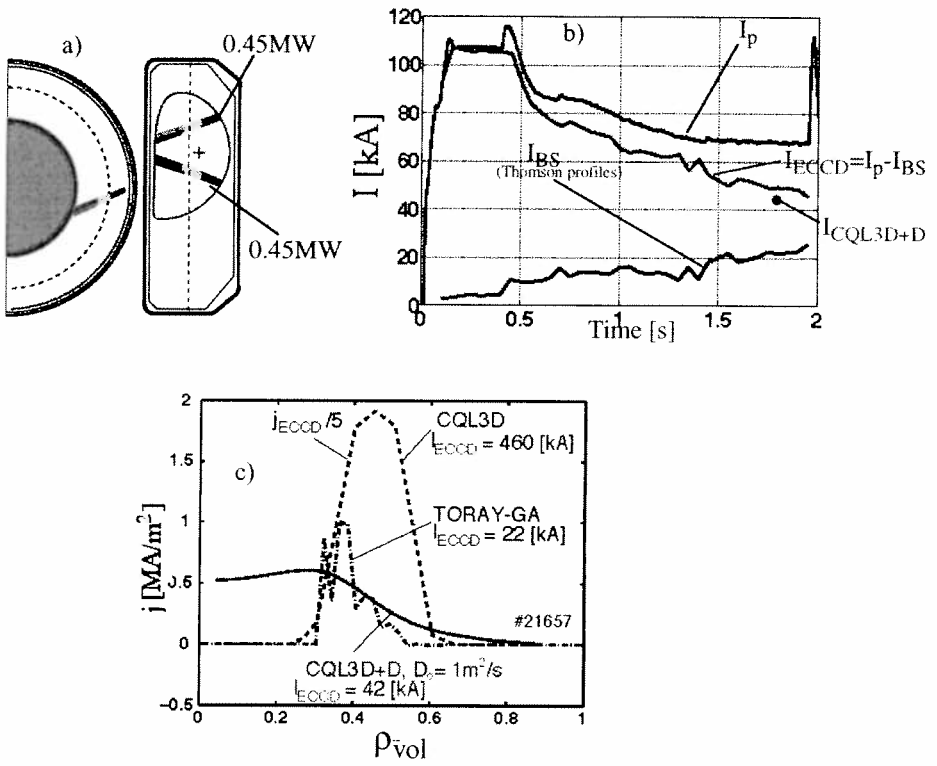

Figure 8. (a) Launching geometry for the co-ECCD beams in a fully ECCD driven plasma (two beams(0.45MW/each) with toroidal injection angle, $\phi = 22^0$). (b) Plasma current (black), bootstrap current (blue) and ECCD driven current(red) time evolutions. The filled red point corresponds to the calculated (CQL3D+D) ECCD driven current with a radial diffusion coefficient $D_0 = 1m^2/s$. A radial dependence of the diffusion coefficient following an L-mode scaling is considered: $D(\rho) = D_0(1+3\rho^3)[n_{e0}/n_e(\rho)]$.(c) Current driven profiles calculated with TORAY-GA, CQL3D, CQL3D+D.

The dominant effect of diffusion at high normalised power density has motivated specific experiments dedicated to the dynamical studies of suprathermal electron relaxation by Modulated ECCD (MECCD) [15]. In these perturbative experiments the response of a high field side ECE radiometer to short, low duty cycle, periodic and localised ECCD has given promising results on the relaxation dynamics of the fast current-carrying electrons. In these experiments, a pulse length of 250μs (duty cycle 1/40), has been empirically adjusted to be well below the time of quasilinear saturation and to permit observation of the spatial propagation of the pulse after rf turn-off. To improve the signal to noise ratio, coherent averaging is performed throughout the steady-state phase of the discharge, comprising up to 200 pulses.

Since for the HFS-ECE, the optical depth of the suprathermal populations is low, and assuming a characteristic temperature of the suprathermal electrons independent of position one can show[15] that the variation of the radiation temperature measured by the HFS-ECE can be directly associated with the variation of suprathermal density. Figure 9(b) shows the time history of the different HFS-ECE channels in response to a short central ECCD pulse with a toroidal injection angle of 25^0 (Figure 9(a)). A simple measurement of the radial

propagation of the pulse is the time to peak calculated from the power turn-off time and is shown on Figure 9(c) for four different shots with increasing vertical distance between the magnetic axis and the horizontal ECE chord.

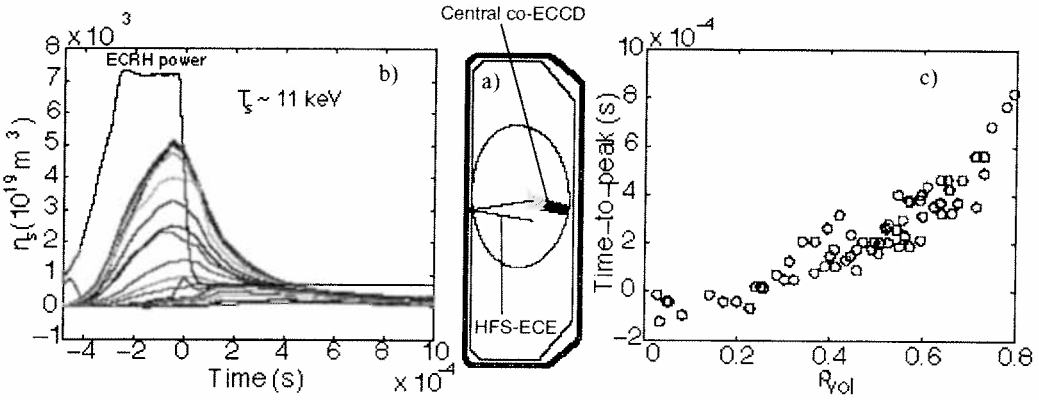

*Figure 9. (a) Configuration of the centrally injected co-ECCD rf beam and the line of sight of the HFS-ECE radiometer. (b) Suprathermal density derived from the HFS-ECE signals, in response to a short central ECCD pulse with a toroidal injection angle of 25^0(ending at t=0), averaged over 114 coherent pulses (shot 25018, I_p = 230kA, $<n_e>$ = 1.5*1019[m^{-3}], T_{epeak}= 1.5keV, κ=1.6). (c) Time-lag from the end of a central ECCD pulse to the ECE peak, as a function of ρ_{vol} calculated by tacking into account the estimated relativistic downshift.*

The TORAY-GA code predicts a power deposition in the region ρ=0-0.2, which is confirmed by the measurements to be a region of zero time-to-peak delay, within the ECE time resolution of 50μs. As for the experimental determination of the power deposition profile with MECH described earlier, the dynamical evolution of this system will be analysed by means of a formal system identification method which allows one to separate the different dynamics associated with this diffusive process. The application of different transport models will possibly allow the determination of the spatial diffusion coefficient of the suprathermal population which will complement the values inferred from the analysis of Hard-X ray emissivity[8].

A final example of the application of co-ECCD in fully non-inductively driven plasmas is described. By staggering different clusters it is possible to extend the plasma discharge to pulse lengths well beyond the limit of 2s for ohmic plasmas. This type of scenario allows one to simulate the maximum reaction time in case of rf power default by imposing a variable time-delay between the turn-off of the first cluster and the turn-on of the second cluster. The situation is shown in Figure 10 a), where the relevant time traces are shown for a complete turn off of the rf power during Δt_{delay} 25ms. The plasma eventually disrupts when the time delay Δt_{delay} is bigger than a maximum value Δt_{max}. The disruption mechanism is a vertical instability occuring while the plasma current is decaying with a constant elongation κ. For a given machine and κ, there is a threshold on the plasma current below which the plasma cannot be maintained. The value of Δt_{max} normalized to the caracteristic decay time of the plasma current (τ =L/R, exponential decay fitting of the plasma current) is shown in Figure 10 b). This result shows that the characteristic time-scale in case of an rf power default has to be faster than the decay time to this Ip-threshold. For the present plasma current levels reached in the experiment this characteristic time scale is of the order of the characteristic L/R decay time of the plasma current.

References

[1] T. Goodmann et al., in Fusion Technology (Proc. 19th Symp. Lisbon 1996), North-Holland, Amsterdam (1997), 565.

[2] J.P. Hogge et al., in Proceedings of 12th Joint Workshop on ECE and ECH (G. Giruzzi editor), World Scientific Publishing, (2002), 371.
Accepted for publication in Nucl. Fusion.

[3] K. Matsuda, IEEE Trans. Plasma Sci. PS-17 (1989) 6.
R.H. Cohen, Nucl. Fusion 30 (1987) 2442.
Y.R. Liu et al. in Controlled Fusion and Plasma physics (Proc. 26th Eur. Conf. Maastricht, 1999), Vol. 23J, European Physical Society, Geneva (1999) 1245.

[4] F. Hofmann and G. Tonetti, Nucl. Fusion 28 (1988) 1871.

[5] S. Alberti et al., Nucl. Fusion 42 (2002) 42.

[6] R. W. Harvey and M. G. McCoy, in Proceedings of the IAEA Technical Committee Meeting on Numerical Mod-eling of Plasmas, Montreal, 1992 (IAEA, Vienna, 1993).
Harvey et al., PRL 62(1989) 426.

[7] Harvey et al., PRL 88(2002).

[8] P.Nikkola et al., in Proceedings of 12th Joint Workshop on ECE and ECH (G. Giruzzi editor), World Scientific Publishing, (2002), 257.
Submitted for publication in Nucl. Fusion.

[9] R. Prater et al., in Proceedings of 15th Topical Conference on radio frequency Power in Plasmas, Moran (Wyoming,USA), May 2003.

[10] T. Goodman., at this workshop

[11] C. Angioni et al, 2003, Nucl. Fusion, 43, 455.

[12] G. Arnoux, at at this workshop

[13] A. Manini et al., Nucl. Fusion 43 (2003), 490.

[14] G. Giruzzi, H. Zohm, ITPA meeting, Naka, 6-8 Feb. 2002, (Japan)

[15] S.Coda et al., Proc. 19th Int. Conf. on Fusion Energy, Lyon, 2002, EX/W-5 (IAEA, to be published); S.Coda et al.,submitted to Nucl. Fusion,
S.Coda et al. Proc. 30th Int. Conf. on Controlled Fusion and Plasma Physics, St. Petersburg, 2003, (EPS, to be published).

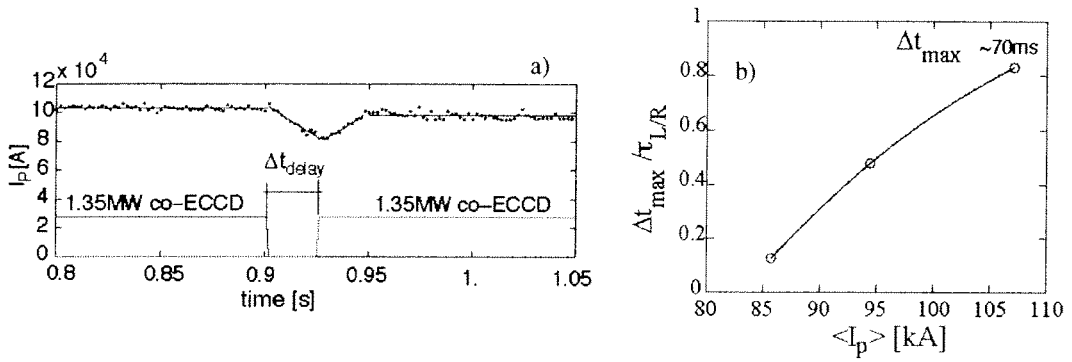

Figure 10. Simulation of rf power default in a fully ECCD driven plasma. (a) Time evolution of the plasma current, co-ECCD rf power during a power default period of Δt_{delay} = 25ms. (b) Maximum delay time, Δt_{max}, normalised to the plasma current decay time(τ =L/R) for different total plasma currents.

Conclusions

Extensive studies with ECH and ECCD on TCV have allowed the validation of different models used to predict the figure of merits of an ECH/ECCD system in terms of localization for both the power deposition and the ECCD driven current. In TCV, the normalised power density as defined by Harvey et al. ranges from values where, for the ECCD driven current calculation, a linear theory (as implemented in the TORAY-GA code) is applicable, to values where non-linear effects and spatial diffusion (Fokker-Planck code, CQL3D + Diffusion) have to be used. For ITER, the normalised power density is very low, such that non-linear and diffusion effects will be negligible and the linear theory will properly predict the ECCD current drive efficiency as well as the current driven profiles. For the high normalised power density experiments on TCV, with significant radial diffusion, dedicated experiments have confirmed the bulk value of the diffusion coefficient and further studies aimed at a direct evaluation of the spatial diffusion coefficient of the fast electrons are currently ongoing.
Limitations for implementing a feedback control on the deposition radius by using a minimum phase criterion (between a spatially resolved diagnostic and MECH) have been analysed. In the case of significant perturbing effects generated by ELM's and/or sawteeth, the phase calculation with an FFT analysis might lead to potential misinterpretations of the deposition radius. In the case of NTM stabilization in ITER, the effects of these perturbations needs to be carefully adressed.

Acknowledgment

This work was supported in part by the Swiss National Science Foundation.

Top-Launch X3 ECH And Its Use As An Electron Energy Diagnostic On The TCV Tokamak

G. Arnoux, S. Alberti, E. Nelson-Melby, L.Porte, P. Blanchard, J.-Ph. Hogge and TCV team.

Centre de Recherches en Physique des Plasmas (CRPP), Association Suisse-Euratom, Ecole Polytechnique Fédérale de Lausanne (EPFL), CH-1015 Lausanne

Abstract: The TCV additional heating system was upgraded with three 450 kW gyrotrons operating at the frequency of 118 GHz for 3rd harmonic X-mode top-launch heating. In the moderate magnetic field of TCV (1.45 T), the X3 ECH system extends the accessible plasma density range to 10^{20} m^{-3}. Since the absorption coefficient is lower with X3 than with X2 by a factor $(k_B T_e)/(m_e c^2)$, a top-launch injection system was installed in order to maximize the ray path length along the resonance layer, thus maximizing the optical thickness. Experiments with a poloidal angle sweep have been performed and showed that the absorption strongly depends on the poloidal injection angle. Optimum absorption was obtained by properly adjusting the launching parameters (poloidal angle and radial position of the mirror). The optimal injection angle is in good agreement with predictions by the linear ray-tracing code TORAY-GA. The need for accurate aiming led us to consider a real time control system, based on a synchronous demodulation technique, to ensure optimal absorption during a discharge with slowly varying parameters (density, temperature, etc.). Preliminary experiments showed that a feedback signal can be obtained from the plasma response (SXR, Te from X-ray, ECE) by modulating the poloidal injection angle.

During the sweep experiments the absorbed power, measured with a diamagnetic loop during a modulated ECH phase (MECH), was observed to be higher than the TORAY-GA predictions. This is attributed to a suprathermal electron population which is observed with the HFS-ECE radiometer. These observations lead us to use the X3 top-launch as a fast electron diagnostic. By varying the radial distance between the RF beam and the cold resonance, the beam can couples selectively to different electron energies. A calculation with a weakly relativistic model assuming a bi-maxwellian distribution function give a vertical single-pass absorption of up to 50% in the HFS region. Preliminary results of this technique and its relevance to the study of the suprathermal electron population will be presented.

1. Introduction

The extension of accessible electron density with the EC system is possible in the moderate magnetic field of TCV (1.45 T) by using a third harmonic X-mode heating. Compared to the 2nd harmonic low field side launch ($ne_{cutoff}=4\cdot10^{19}$ m^{-3}), the third harmonic extends to the cutoff density $ne_{cutoff}=12\cdot10^{19}$ m^{-3} and allows the heating of H-mode plasmas [1]. The low X3 absorption coefficient has led us to choose an upper launcher in order to maximize the beam path along the resonance, that is to maximize the optical depth. The X3 heating system on TCV is composed of three 450 kW gyrotrons operating at the frequency of 118 GHz. The X3 launcher is an elliptical mirror focusing in the center of the plasma. Its poloidal angle can vary from 40° to 50° during the discharge at a maximal velocity of 20 deg/s.

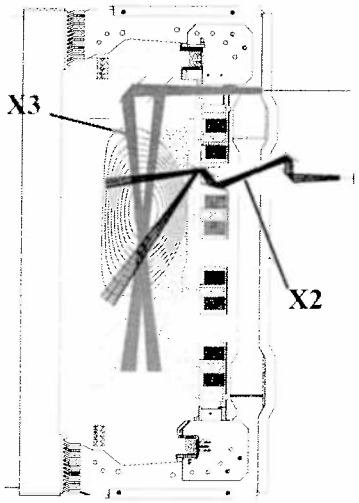

Figure 1: Poloidal view of the TCV vessel with both X2 and X3 beam.

The mirror can move radially between 80 and 97 cm (as shown in Figure 1) from shot to shot [2].

In this paper, section 2 discusses the absorption properties of X3 top-launch on the base of theoretical results. Section 3 presents the observations made during poloidal launcher angle sweep. The absorption efficiency depends strongly on the poloidal injection angle and this is in good agreement with predictions of the linear ray-tracing code TORAY-GA. The sweep method allows us determining the optimal injection angle and TORAY-GA is a useful tool to predict the optimum injection angle. Since the X3 absorption depends strongly on the poloidal angle and since the optimum angle varies during a discharge (Temperature and density variations), a real time feed back control on X3 launcher has been proposed. Section 4 shows the feasibility and a simulation of such a control system. Section 5 presents X3 heating experiments showing the role played by the suprathermal electrons in the X3 absorption efficiency. Therefor the X3 heating can be used as a fast electron diagnostic in a purely vertical launch by exploiting the relativistic shift effect. Preliminary experiment has shown the potential of such a diagnostic.

2. X3 absorption coefficient and sensitivity with top-launch

In a weakly relativistic approximation and for the finite density regime $(\omega_p/\omega_c)^2 \gg 2(v_{th}/c)^2$, the absorption coefficient of the third harmonic, for an extraordinary polarization mode (X-mode) and in a quasi perpendicular propagation, is given by

$$\alpha_3^{(X)} = \left(\frac{3}{2}\right)^4 \left(\frac{\omega_p}{\omega_c}\right)^2 \left(\frac{v_{th}}{c}\right)^2 \left| 1 - \frac{\omega_p^2}{3(8\omega_p^2 - \omega_c^2)} \right|^2 \cdot N_{\perp,c}^3 [-F''_{9/2}(z_3)] \tag{2.1}$$

where ω_p is the plasma frequency, ω_c is the cyclotron frequency, v_{th} is the electron thermal velocity and $N_{\perp,c}$ is the real part of refractive index (given by the Happleton-Hartree dispersion relation) [3]. $F''_{9/2}(z_3)$ is the imaginary part of the Dnestrovsky function (Shkarovsky function for perpendicular propagation) and the variable z_n is such that

$$z_n = \left(\frac{c}{v_{th}}\right)^2 \cdot \frac{\omega - n\omega_c}{\omega}. \tag{2.2}$$

with n=3. In comparison to the second harmonic, the X3 absorption coefficient is lower by a factor:

$$\frac{\alpha_3^{(X)}}{\alpha_2^{(X)}} \approx \left(\frac{v_{th}}{c}\right)^2 = \frac{Te\ [\mathrm{keV}]}{511} \tag{2.3}$$

and in order to maximize the optical depth $\tau_{X3} = \int \alpha_3^{(X)} ds$ a top-launch is required. In a top-launch configuration, the optical depth $\tau_{X3}^{TOP} \approx n_e T_e$ in the case where the wave vector stays quasi parallel to the resonance layer, whereas for a low-field-side launch, the optical depth $\tau_{X3}^{LFS} \approx n_e T_e^2$. Figure 2 shows the absorption coefficient as a function of the minor radius (magnetic field dependence) for three different temperatures and for a density n_e=3·10^{19} m^{-3}. The amplitude of the absorption coefficient is linearly dependent on the temperature. The resonance layer defined as the full width at half maximum (FWHM) of the absorption coefficient also increases linearly with the temperature. In a top launch configuration, such a broadening

decreases the absorption sensitivity on the poloidal injection angle depending also on the beam size. For X3 low-field-side launch, it would increase the optical depth, whereas for X2 low-field-side launch, it has not any effect because the power is fully absorbed before to reach the maximum of $\alpha_2^{(X)}$. The distance ΔR between the cold resonance and the maximum of $\alpha_3^{(X)}$ is shifted towards the high field side (HFS) as the temperature increases. This shift can strongly affect the absorption efficiency in a vertical launch configuration since the beam path can get out from the resonance layer. In the case of X2 ECH or ECCD, the high absorption makes that the shift of the absorption coefficient to the high field side is of second order and becomes relevant for studies on decrease of trapping for off-axis ECCD as studied by Prater et al. [4] Both broadening and shift

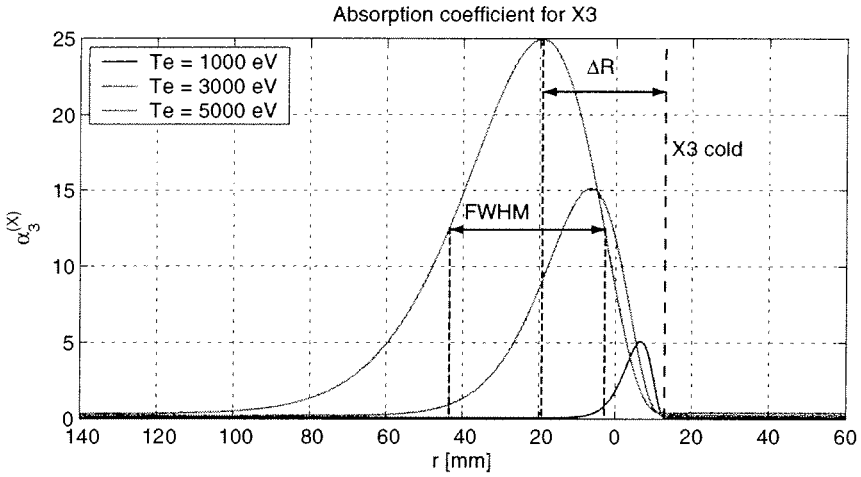

Figure 2: The X3 absorption coefficient versus the minor radius. The amplitude, the Full Width at Half Maximum w (FWHM) as well as the distance between the maximum and the X3 cold resonance ΔR increase with the temperature.

effects on X3 top-launch absorption can be associated to the poloidal injection angle sensitivity. The broadening effect can be evaluated by assuming that if the maximum of the absorption coefficient is reached when θ_l=45° (vertical launch), the angle sensitivity is defined by the angle necessary to reach the FWHM w. By taking a typical plasma target which gives the vertical distance Δz=767 mm between the launcher and the plasma center, the angle sensitivity is such that $\tan(\theta_l - 45) = w/(2\Delta z)$ and one finds $d\theta_l/dTe$ =0.3 deg/keV. The shift effect is evaluated by assuming that if the vertical launch (θ_l=45°) is such that the beam follows the X3 cold resonance, the angle sensitivity is taken to be the angle necessary to reach the maximum of the absorption coefficient: $\tan(\theta_l - 90) = (\Delta R)/(\Delta z)$. By taking the same Δz, one finds that $d\theta_l/dTe$ =0.25 deg/keV. The real sensitivity is not so limiting because the beam size smooths both shift and broadening effect. The beam size is characterized by its wait w_0=21 mm (E-field), that is the beam diameter is 42 mm and is equal to the resonance layer w for a temperature of 5 keV.

3. Poloidal injection angle dependence of X3 top-launch absorption

In order to study the X3 absorption sensitivity on the mirror poloidal angle, experiments using a poloidal angle sweep have been performed. The soft X-ray emission from a central chord has been used to determine the absorption sensitivity on the injection angle. The experiments have been performed at central densities in the range $3.5 \cdot 10^{19}$ to $8.4 \cdot 10^{19}$ m^{-3}. The soft X-ray signal is proportional to $n_e^2 T_e$ and it has been verified that the main effect on the signal variation is related to a temperature variation. Figure 3 shows the soft X-ray emission and the single-pass absorption, calculated using the linear ray-tracing code TORAY-GA versus poloidal mirror angle. The typical width characterizing the absorption sensitivity corresponds to a mirror angle variation $\Delta\theta_l \approx 1^o$ (FWHM). A deviation of 1^o from the optimum angle causes the TORAY-GA absorption to decrease to zero. The maximum of the measured signal and TORAY-GA maximum are in good agreement. Therefore it is a good tool to predict the optimum angle, but since the optimal angle changes with temperature and/or with density variations, a real-time feed back control is necessary.

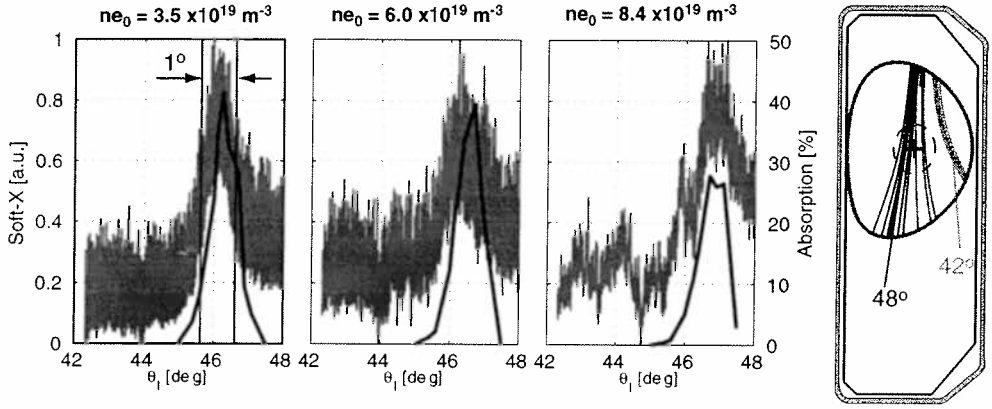

Figure 3: SXR emission from a central chord and X3 absorption predicted by TORAY-GA versus poloidal mirror angle for three different central densities. On the left, a poloidal view of the vessel illustrates the beam path during the sweep of the launcher angle from 42^o to 48^o.

First experiments and simulation have been conducted in order to study the feasibility of such a control on TCV.

4. Real time control of X3 launcher angle

The goal of a real time control is to optimize the absorption using a dynamic response from the plasma produced using a small perturbation. The perturbation is performed by modulating the poloidal angle of the mirror at frequencies between 30 Hz and 70 Hz (technical limits). The optimum angle can be extracted from the dynamic response of the plasma using appropriate signal processing. Poloidal injection angle modulations have been done on TCV and the plasma

response has been measured on a central vertical chord of the soft X-ray emission. Figure 4 a) shows the launcher modulation given by

$$\theta(t) = \theta_0(t) + \delta\theta\cos(\omega_{mod}t) \tag{4.1}$$

where $\delta\theta$=0.2° and $\omega_{mod}/(2\pi)$=40 Hz. θ_0 denotes the slow variation which is, in Figure 4 a), time proportional in the angle range 45° to 47°. Figure 4 b) shows the raw signal of the dynamic plasma response. Its slow variation can be modelized by a gaussian function and the perturbation is visible. Figure 4 c) shows the AC component of both perturbation and response signal after digital signal processing. The amplitude of the plasma response becomes zero at the optimal angle corresponding to the maximum of the SXR signal. The phase, shown on Figure 4 d), between the perturbation and the plasma response jump from 0 to 180° at the maximum of the SXR signal. The optimal injection angle can be accurately determined using the phase jump. The modulation

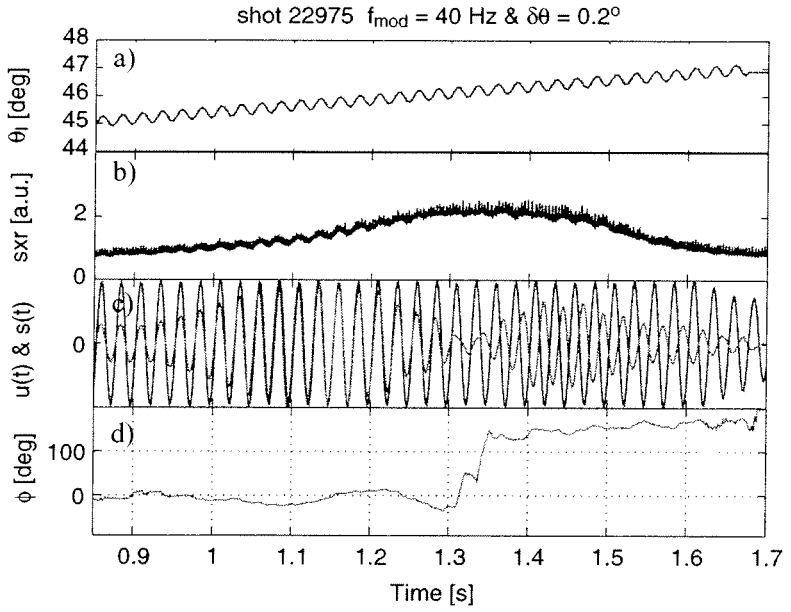

Figure 4: a) the mirror poloidal angle modulation added to a slow variations (sweep), b) SXR signal from a central chord reacting to the perturbation, c) AC component of both perturbation u(t) and plasma response s(t) obtained by digital signal processing and d) phase between u(t) and s(t). The modulation is such that $\delta\theta$=0.2° and f_{mod}=40 Hz. The angle is in the range 45° to 47° (LFS to HFS) in order to sweep over the maximum absorption.

frequency of 40 Hz is the minimum required to ensure that the phase shift is initially zero. In order to get a fast reaction time, the modulation frequency should be increased but this is possible only of the modulation amplitude is decreased (technical limits). This will be possible taking into account the experimental results.

The feed back control system has been simulated using the Matlab package SIMULINK. Such a system can be divided in five parts as shown in the block diagram of Figure 5. The first part

(Figure 5 a)) is the sinusoidal modulation of the mirror as defined in (4.1). The second part (Figure 5 b)) builds the response signal such that

$$s(t) = s_0 \exp\left\{-\left(\frac{\theta(t)-\bar{\theta}}{\sigma_\theta}\right)^2\right\} + \Gamma_0 \cong s_0\left[\exp\left\{-\left(\frac{\theta_0(t)-\bar{\theta}}{\sigma_\theta}\right)^2\right\} + \frac{ds}{d\theta}\delta\theta\cos(\omega_{mod}t)\right] + \Gamma_0 \quad (4.2)$$

where $\bar{\theta}$ is the optimum angle, σ_θ denotes the absorption sensitivity (~0.7 times the FWHM) and Γ_0 is a random fluctuation function. The third block (Figure 5 c)) executes the synchronous demodulation using the plasma response and the reference signal and gives the derivative of the signal $ds/d\theta$. The output signal is fed through a PID controller (Figure 5 d)) which builds the error signal. The term proportional to $ds/d\theta$ (P) allows getting close to the optimal angle but not remaining on. The integration term (I) allows reaching the optimal angle and staying on with an accuracy $\delta\theta$. The last part (Figure 5 e)) defines the starting angle $\theta_0(t=0)$ and allows simulating a

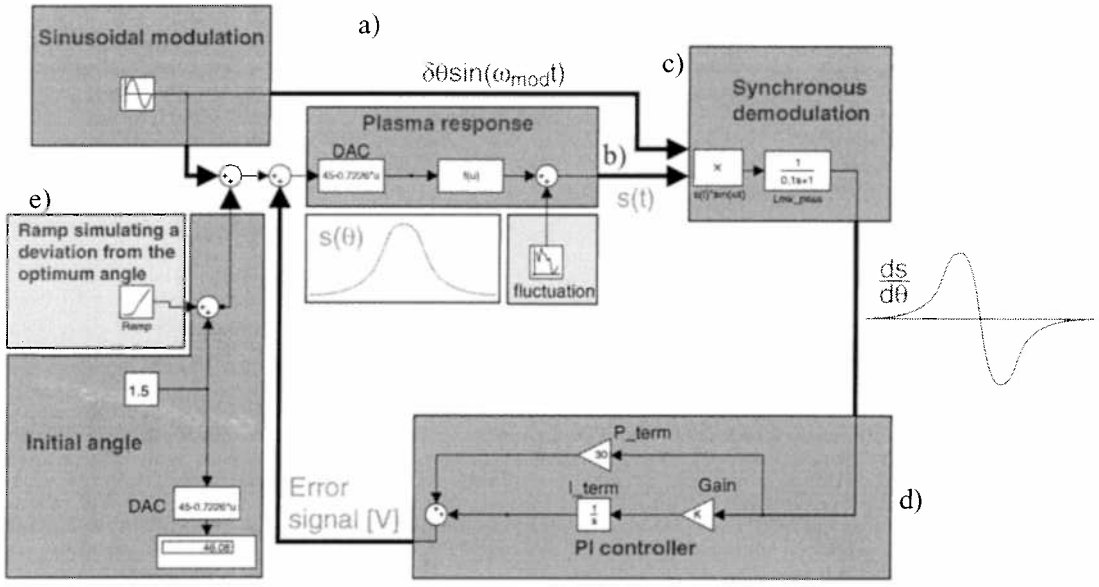

Figure 5: Block diagram of the simulated feed back control. a) the reference signal (sinusoidal modulation), b) the plasma response is define as a gaussian function of the mirror angle, c) the synchronous demodulation gives the signal slope, d) the proportional-integrator (PI) controller giving the error signal and e) the starting angle and a deviation from the optimum injection angle simulating variations in plasma parameters.

deviation (slow variation of $\theta_0(t)$) from the optimal angle, which could be due to temperature or density variations. Figure 6 shows the control system dynamic for the following parameters: the optimal angle is $\bar{\theta} = 45°$, the modulation amplitude $\delta\theta=0.15°$, the modulation frequency $f_{mod}=\omega_{mod}/2\pi=70$ Hz and the random fluctuations are 10% of the output signal $s(t)$. Figure 6 a) shows that the starting angle $\theta_0(t<1) = 46°$ and after 1 s, a deviation is imposed such that $\theta_0(t>1)$ deviates by 2 deg/s. Figure 6 b) shows the error signal which is characterized by three typical times. The rise time $T_{ri} = 130$ ms is the time that the system needs to rise from 10% to 90% of the final value. The peak time $T_p = 220$ ms is the time that the system takes to reach the first maxi-

mum of oscillations around the final value. The settling time T_s = 440 ms is the time that takes the system to oscillate within 2% of the final value. Figure 6 c) shows the launcher angle according to the error signal. The angle fluctuates around the optimal angle (45°) within 0.15°, even when the deviation is imposed. In the present configuration ($\delta\theta$ = 0.15 and $\omega/(2\pi)$=70 Hz), the system can compensate the imposed deviations up to 20 deg/s (it corresponds to the speed limit of the launcher) and is able to reach the optimal value in the 2 seconds time window by starting from the maximum value $\theta_0(0) = 46.16^o$. This means that the starting angle has not to exceed 1° from the optimal angle since the feed back is wanted to be in the typical time scale of TCV.

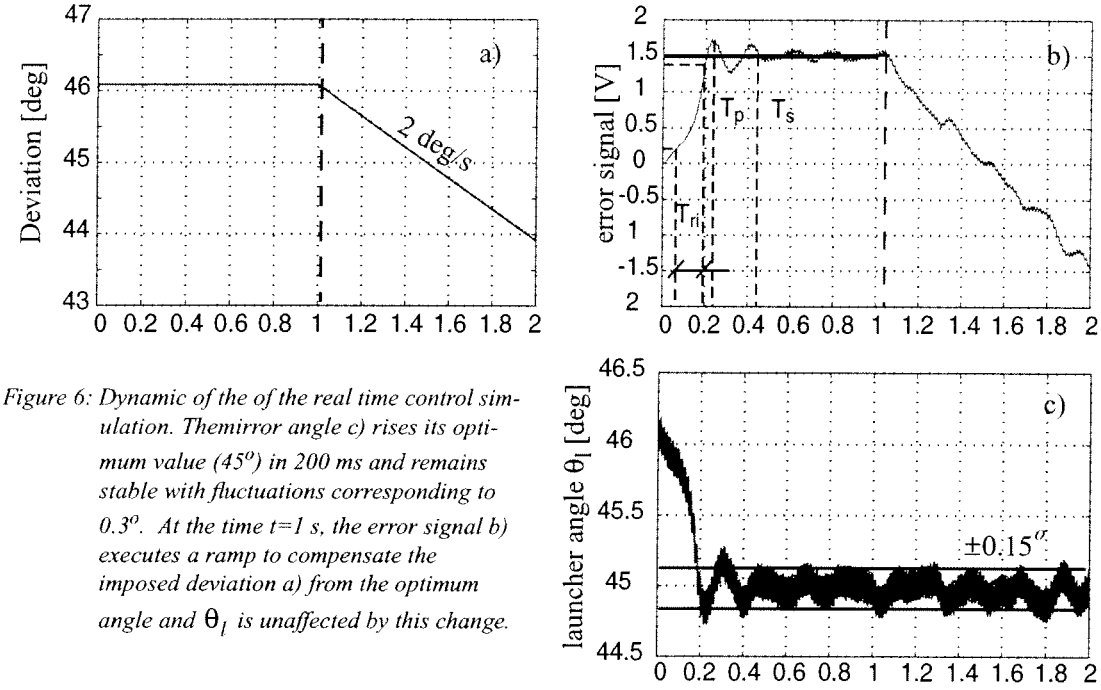

Figure 6: Dynamic of the of the real time control simulation. Themirror angle c) rises its optimum value (45°) in 200 ms and remains stable with fluctuations corresponding to 0.3°. At the time t=1 s, the error signal b) executes a ramp to compensate the imposed deviation a) from the optimum angle and θ_l is unaffected by this change.

In this section, a first step has shown that an exploitable signal from the dynamic response of the plasma can be obtained and a second step has shown, with a simulation, that this system is sufficiently fast and stable to be implemented on TCV. In conclusion, it has been demonstrated that a real time feed back control is feasible on the X3 launcher. A real time controller is being implemented on TCV and experiments using the controller will begin in september.

5. X3 heating and fast electrons

In the frame of X3 absorption optimization experiments, comparisons between the absorption measurements and the TORAY-GA predictions have been performed. In these set of experiments, 1 MW of X3 power was injected into a plasma target as illustrated in Figure 7. The X3 absorption measurement is performed by square wave modulating one gyrotron (450 kW) at 237 Hz between 1.2 and 1.5 seconds. The absorbed power is deduced from the induced variation of

the diamagnetic flux measured with a diamagnetic loop (DML) [5]. Figure 7 shows that X3 heating makes the central temperature (From Thomson scattering) increase from 1 keV to 2 keV. The DML measurement gives an absorption of 65% (averaged on the modulation time window) whereas the TORAY-GA predictions give an absorption of 40%. This discrepancy can be explained by the presence of a non negligible population of suprathermal electrons and has been observed in more complex scenarios like high elongated plasma with far off axis X2 ECH [6] or LFS injection of X3 with X2 EC pre-heating [7]. At the RF power switch on, the high field side ECE (HFS-ECE) signal increases. This is a signature of the presence of suprathermal electrons since this signal should be in the cutoff, that is the signal should be flat because the 2nd harmonic emission from the bulk should be completely reflected since it comes from the center. It has been shown that the fast electrons play a role in the X3 absorption [8].

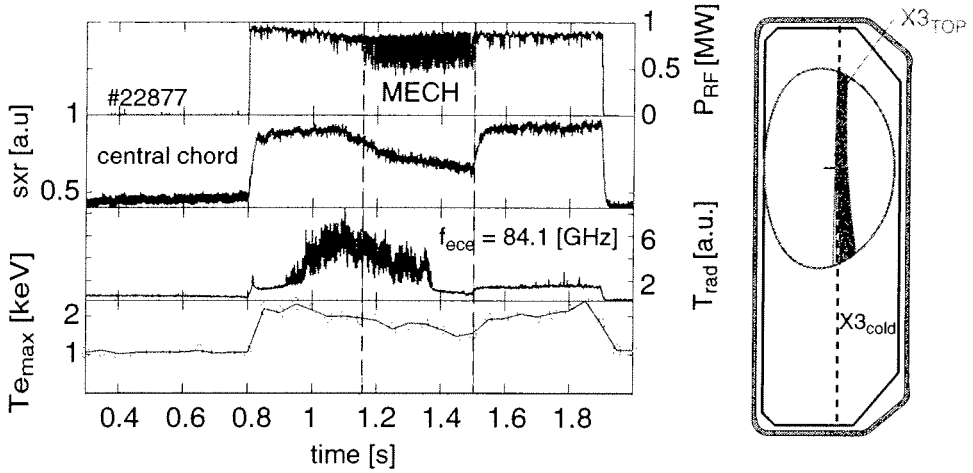

Figure 7: Typical scenario with 1 MW X3 top-launch heating. The absorption measurement during the square wave power modulation (MECH between 1.2-1.5 s) gives an absorption of 65%. The high field side ECE measurement is representative of the suprathermal population since it should be in the cutoff. The maximum temperature from Thomson scattering increases from 1 keV to 2 keV at X3 switch-on. On the left, the beam path is quasi-vertical along the cold resonance.

The strong coupling of X3, launched from the top, with the suprathermal electrons observed in these preliminary experiments suggests its use as a fast electrons diagnostic. In a pure vertical launch, the radial distance R of the X3 launcher with respect to the cold resonance is directly linked to the energy of the coupled electrons. In a pure heating, from the relativistic shift effect, the energy of a single resonant particle is given by

$$E(R) = \left(\frac{n\omega_c(R)}{\omega} - 1\right) \cdot m_e c^2 \qquad (5.1)$$

where n=3. Figure 8 b) shows the effect of the suprathermal population on the X3 absorption in a vertical single-ray path. This calculation has been done by assuming a bi-maxwellian distribution function and parabolic profiles $A(r) = A_0(1-(r^2/a^2))^{\alpha}$ with different peaking coefficient α.

The plasma bulk temperature and density as well as the plasma geometry are the same for all curves. The fast electrons temperature is respectively 21 keV for the dark-blue curve and 35 keV for the light-blue curve. The central bulk temperature Te_0=2 keV and the red curve represents the absorbed fraction without suprathermal tail. The X3 absorption can reach 60% if the suprathermal density is 10% of the total density and if the suprathermal temperature is 12 keV. By scanning the radial position of the X3 launcher, the RF beam can selectively couple on the different energies and such an absorption curve as shown in Figure 8 b) should be reproduced. The radial scan experiments have been performed by generating fast electrons with 100 kW of X2 CO-ECCD. Figure 8 a) shows poloidal and top view of both X2 and X3 beam trajectories. In these preliminary experiments, the density was chosen too high ($ne_0 \sim 3 \cdot 10^{19}$ m^{-3}) and refraction of the X2

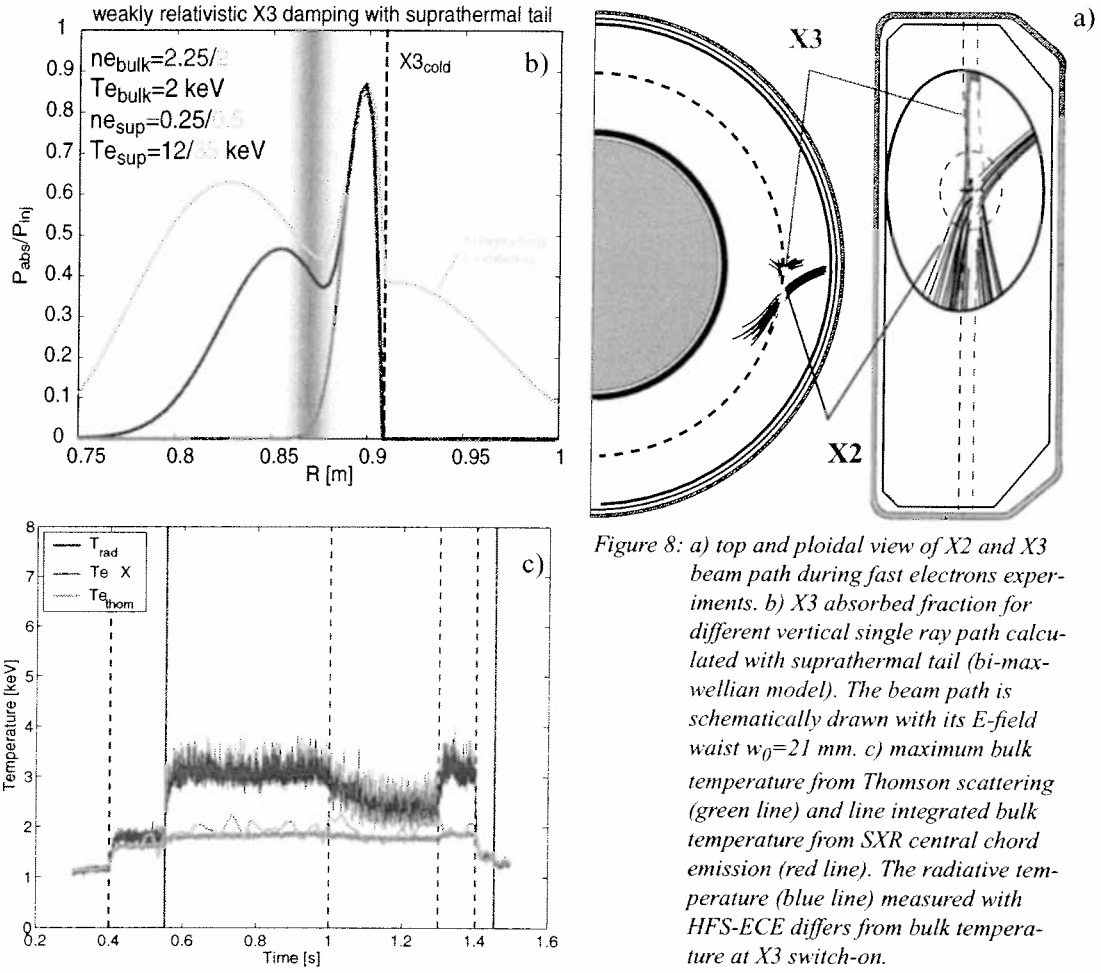

Figure 8: a) top and ploidal view of X2 and X3 beam path during fast electrons experiments. b) X3 absorbed fraction for different vertical single ray path calculated with suprathermal tail (bi-maxwellian model). The beam path is schematically drawn with its E-field waist w_0=21 mm. c) maximum bulk temperature from Thomson scattering (green line) and line integrated bulk temperature from SXR central chord emission (red line). The radiative temperature (blue line) measured with HFS-ECE differs from bulk temperature at X3 switch-on.

beam trajectory degrades the CD efficiency. On the other hand, the X3 beam is unaffected and its trajectory remains vertical. The energy selectivity is related to the X3 beam waist (w_0=21 mm E-field) which corresponds to an electron energy ΔE=12 keV. With a launcher radial position R=870 mm, as schematically drawn on Figure 8 b), TORAY-GA predicts no X3 absorption, that is X3

doesn't couple with the bulk, whereas the DML measurements gives an absorption of 25%. The X3 power is thus fully absorbed on suprathermal electrons which have an energy $E = 26 \pm 12$ keV. This interpretation is confirmed by the radiative temperature increase from 2 keV to 3 keV at the X3 switch-on as shown in Figure 8 c). With a launcher radial position R=890 mm, TORAY-GA and the DML measurements give both 45% of X3 absorption, that is the beam couples only on the bulk. Nevertheless the radiative temperature increases from 2 to 5 keV which denotes the generation of suprathermal electrons and since the beam couples the bulk, it is not able to increase the fast electrons energy. Future experiments will be conducted to scan a broader energy range, with a lower density and with higher X2-ECCD power level.

6. Conclusion

The necessity for a real time feed back control on the X3 upper launcher, based on the observed sensitivity of X3 absorption on mirror angle, has been established and its feasibility on TCV has been demonstrated. Since it is accurate enough with respect to the X3 top-launch absorption sensitivity, such a control system will be implemented.

X3 top-launch heating experiments have shown that suprathermal electrons play a role in the X3 absorption efficiency. The upper configuration of the launcher allows, by vertical injection, to couple selectively different electron energies and thus make X3 top-launch a useful tool as a fast electron diagnostic. The study of the fast electron population is motivated by the fact that the X3 absorption properties can be significantly modified.

For Neoclassical Tearing Mode (NTM) stabilization, injection of O1 ECH from upper launcher in ITER is foreseen. Such a stabilization system needs a real time feed back control. It also requires a minimum accuracy for the mirror orientation since the deposition location must be controlled. Figure 9 shows a shematic view of ITER plasma with upper launcher and O1 cold resonance. This picture can be used to evaluate the poloidal injection angle accuracy. The characteristic deposition width given by a NTM island size of δz=18 cm ($\delta r/a$=0.05) defines the angular

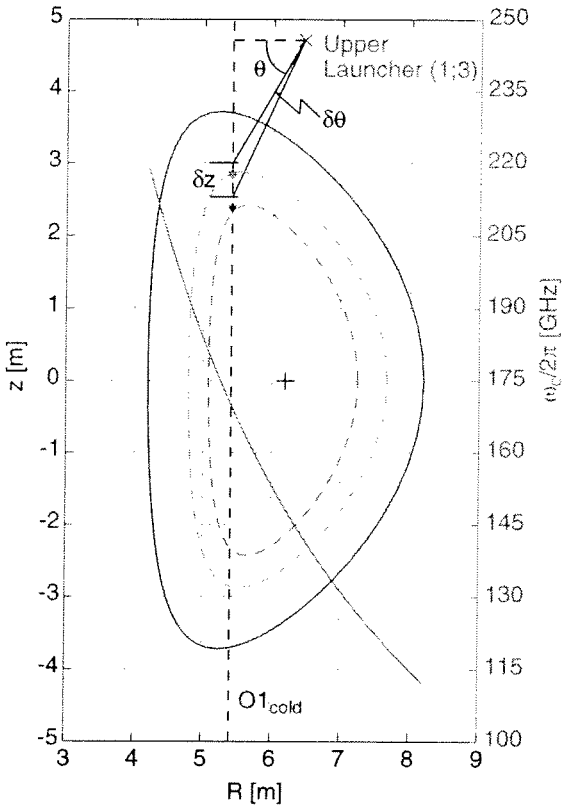

Figure 9: ITER poloidal view with upper ECH launcher. The launcher accuracy δθ is evaluated, considering a 2 dimensional geometry (restricted to the poloidal x-section), for poloidal injection angle θ necessary to reach both q=3/2 and q=2 surfaces. The deposition width is δz=18 cm and corresponds to δr/a=0.05.

aiming accuracy of the top launch. Considering the plasma and launching geometry given in reference [9], the required angle accuracy is $\delta\theta$=2.3 and $\delta\theta$=1.6 for q=2 (r/a=0.66) and q=3/2 (r/a=0.79) respectively. The TCV upper launcher accuracy is significantly higher than this requirement and the future feed back control system on TCV will give useful preliminary results.

7. References

[1] L. Porte, S. Alberti, G. Arnoux, Y. MArtin, J.-Ph. Hogge, T. P. Goodman, M. A. Henderson, E. Nelson-Melby, A. Pochelon, M.Q. Tran, *Third harmonic X-mode electron cyclotron resonance heating on TCV using top launch*, IAEA-CN-94, Lyon (2002).

[2] J.-Ph. Hogge, S. Alberti, L. Porte, and G. Arnoux, *Preliminary results of top launch 3rd harmonic X-mode electron cyclotron heating in the TCV Tokamak*, IAEA (2002) Vienna.

[3] M. Bornatici et al., *Electron cyclotron emission and absorption in fusion plasmas*, Nucl. Fusion **23** (9), 1983.

[4] R. Prater et al., *Decrease in trapping effects for off-axis electron cyclotron current drive in high performance plasmas*, 14th conference on radio frequency power in plasmas, Oxnard California, 2001, pp 302-305.

[5] A. Manini, J.-M. Moret, S. Alberti, T. P. Goodman and M. A. Henderson, *Modulated ECH power absorption measurement using a diamagnetic loop in the TCV Tokamak*, Plasma Phys. Control. Fusion **44**, 2002, pp. 137-157.

[6] A. Pochelon et al., *ECH power deposition at 3rd harmonic in high elongation TCV discharges sustained by 2nd harmonic current profile broadening*, 19th IAEA Fusion Energy Conference Lyon, 2002.

[7] S. Alberti et al., *Full absorption of third harmonic ECH in TCV tokamak plasmas in presence of second harmonic ECCD*, Nucl. Fusion **42** (1), 2002, pp 42-45.

[8] P. Blanchard, S. Alberti, S. Coda, H. Weisen, P. Nikkola and I. Klimanov, *High field side measurements of non-thermal electron cyclotron emission on TCV plasmas with ECH and ECCD,* Plasma Phys. Control. Fusion **44**, 2002, pp. 2231-2249.

[9] B. Lloyd, C. Warrick and M. O'Brien, *Performance of the ITER ECRF launchers*, Final report in ITER design task (contract EFDA 00/549), August 2002.

Electron Heat Transport Studies Under Intense EC Heating in TCV

Y. Camenen[1], A. Pochelon[1], F. Ryter[2], S. Coda[1]

[1]*Centre de Recherches en Physique des Plasmas CRPP EPFL, Association EURATOM-Confédération Suisse, Lausanne, Switzerland.*
[2]*Max-Planck-Institut für Plasmaphysik, EURATOM-IPP Association, Garching, Germany.*

1. Introduction

Plasma turbulence is generally thought to be responsible for anomalous cross-field electron heat transport which typically exceeds by two orders of magnitude the neoclassical transport in tokamak L-mode discharges. In particular, electron temperature gradient (ETG) modes and trapped electron modes (TEM) are candidate causes of anomalous transport as they are theoretically predicted to exhibit a threshold in $\nabla T_e/T_e$ which is consistent with the experimental profile resilience or stiffness observed in many tokamaks during the last three decades [1]. Above the threshold, an increase of the heat flux leads to a large increase of radial transport which acts such as to keep the logarithmic gradient of T_e almost unchanged. Moreover, the value of $R\nabla T_e/T_e$ is quite comparable in several tokamaks, which suggests the same underlying turbulence.

TCV experiments with varying $\nabla T_e/T_e$ and constant edge heat flux at two different plasma triangularities (δ~0.2 and δ~0.4) are discussed in this paper. The dependence of the electron thermal diffusivity χ_e on $\nabla T_e/T_e$ is investigated. Thanks to a flexible electron cyclotron heating system combined with the highest EC power densities used in such experiments to date, $\nabla T_e/T_e$ is forced to extremely high values. The dependence of the electron thermal diffusivity χ_e on $\nabla T_e/T_e$ is compared to that found in ASDEX Upgrade [2] and to a model used in ASDEX Upgrade and JET [3, 4].

2. Description of the experiments

In the TCV tokamak (major radius R_0=0.88m, minor radius a<0.255m, magnetic field B_T<1.54T) auxiliary heating relies on an ECH system totalling 4.5MW of nominal power for a 2s pulse length. The 2nd harmonic frequency ECH system (X2) is composed of six gyrotrons at 82.7GHz and six independent low field side launchers steerable during the discharge, delivering a total nominal power of 3MW. The 3rd harmonic frequency ECH system (X3) consists of three

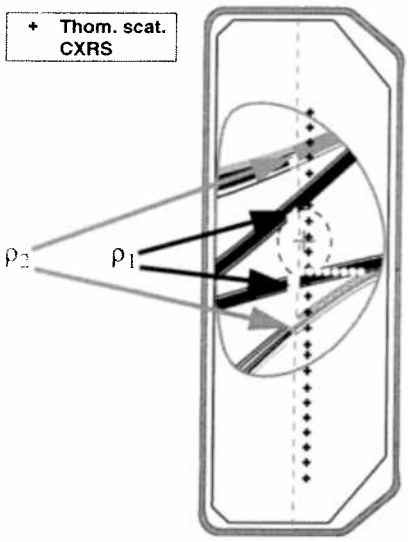

Figure 1:

Poloidal view of the plasma cross section and of the EC beams for the two deposition location ρ_1 and ρ_2.

The cold resonance is indicated by the red dashed line.

The Thomson scattering and Charge Exchange Recombination Spectroscopy (CXRS) measurements location are indicated by black crosses and green dots, respectively.

I_p~220kA, B_T=1.44T, q_{95}~5.4, κ~1.6, δ~0.4

gyrotrons at 118GHz, with a single top launcher that can also be steered during the discharge, delivering a total nominal power of 1.5MW.

In the present experiments, the plasma current and magnetic field are I_p~220kA and B_T=1.44T. The edge elongation κ is approximately 1.6 and two triangularities, δ~0.2 and δ~0.4, are explored with a safety factor q_{95} of 4.7 and 5.4, respectively. The X2 ECH system is used to deposit from 0.45 to 1.8MW of EC power (X2) at two different normalized radii, $\rho_1 \sim 0.35$ and $\rho_2 \sim 0.7$, in a L-mode plasma in limiter configuration. The normalized radius is defined as $\rho = \sqrt{V/V_{LCFS}}$, where V is the plasma volume. A poloidal view of the plasma cross-section and of the EC beams aiming at ρ_1 and ρ_2 is shown in **Fig 1**. The single pass absorption is ~100% (T_{eo}~1.5-4.5keV, n_{eo}~1.3-2.4x10^{19}m^{-3}) and refraction effects are weak, since $n_{eo}/n_{e\ \text{cut-off}} < 0.6$, which results in a narrow deposition region and therefore high power densities, up to 7MW/m^3.

Keeping the total EC power $P_{EC}(\rho_1) + P_{EC}(\rho_2)$ constant and varying the EC power deposition distribution, $P_{EC}(\rho_1)/P_{EC}(\rho_2)$, the electron heat flux Q_e between ρ_1 and ρ_2 and therefore the electron temperature gradient ∇T_e are changed at constant edge heat flux.

The profiles of the electron temperature T_e and density n_e are obtained every 25ms from a Thomson scattering diagnostic covering the full plasma height with a spatial resolution of 4.5cm. The T_e and n_e profiles are measured after steady state is reached and averaged over ~300ms. This leads to the relatively small error bars for T_e shown in the figures. The normalized temperature gradient $R/L_{Te} \equiv (R\nabla T_e/T_e)$ is calculated at the low field side mid-plane. The ion temperature profile T_i is obtained from a Charge Exchange Recombination Spectroscopy (CXRS) every 150ms [5]. The plasma region seen by the two diagnostics is indicated in **Fig 1**.

3. Temperature profile variations

As shown in **Fig 2**, the shape of the T_e profile does not depend on the amount of centrally deposited EC power. Here, $\rho_{dep} = \rho_1$. As the deposited EC power is varied from 0.45 to 1.8MW,

∇T_e and T_e^{edge} increase, but R/L_{T_e} only varies by 10% in the region $\rho_1 < \rho < \rho_2$. This was already observed in the past in several tokamaks and is known as profile resilience or stiffness [1, 6].

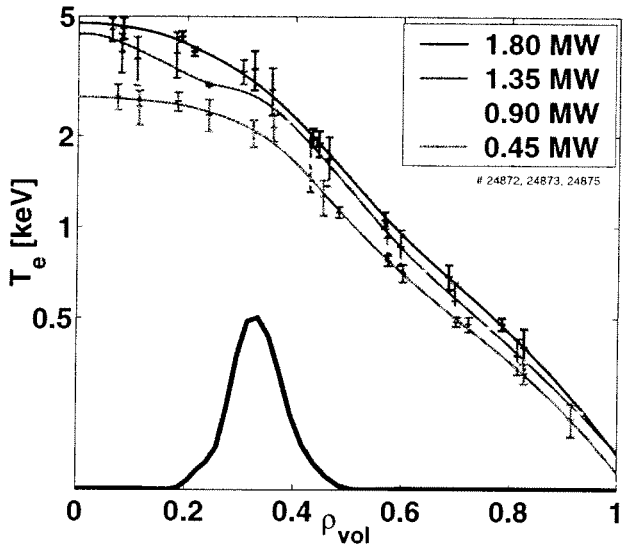

Figure 2:

T_e profile in logarithmic scale. The EC power is varied from 0.45MW to 1.8MW at constant deposition location, ρ_1~0.35, indicated in arbitrary units by the thick blue line.

The T_e profile is stiff for 0.4<ρ<0.7.

δ~0.2.

On the contrary, a change of the EC power deposition distribution $P_{EC}(\rho_1)/P_{EC}(\rho_2)$ at constant total EC power leads to large variations of R/L_{T_e} as illustrated in **Fig 3a** and **Fig 3b**. Here, T_e^{edge} remains constant while the EC power distribution is changed because the flux surface averaged electron edge heat flux Q_e^{edge} is kept constant. For a total EC power of 1.8MW, which corresponds to a value of Q_e^{edge} of approximately 0.15MW/m^2, R/L_{T_e} varies by a factor 5. The

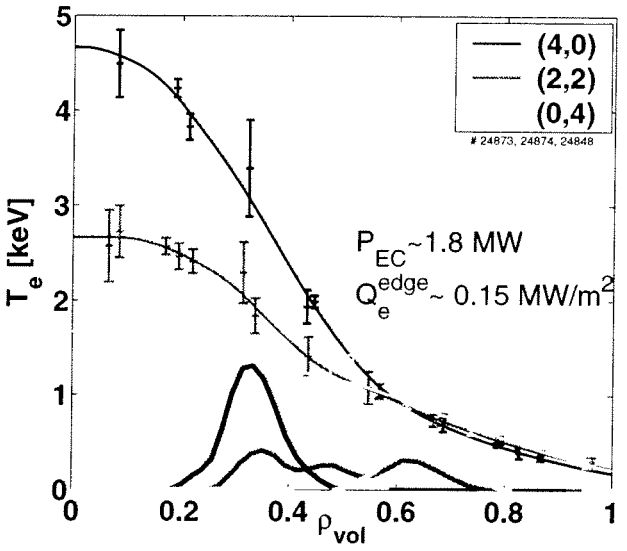

Figure 3a:

T_e profile variation at constant total EC power (P_{EC}~1.8MW) for different radial distributions of the EC power.

The EC power deposition is indicated in arbitrary units by the thick lines.

The two numbers in the legend, represent the number of EC beams aimed at ρ_1 and ρ_2, respectively (0.45MW per beam).

δ~0.2.

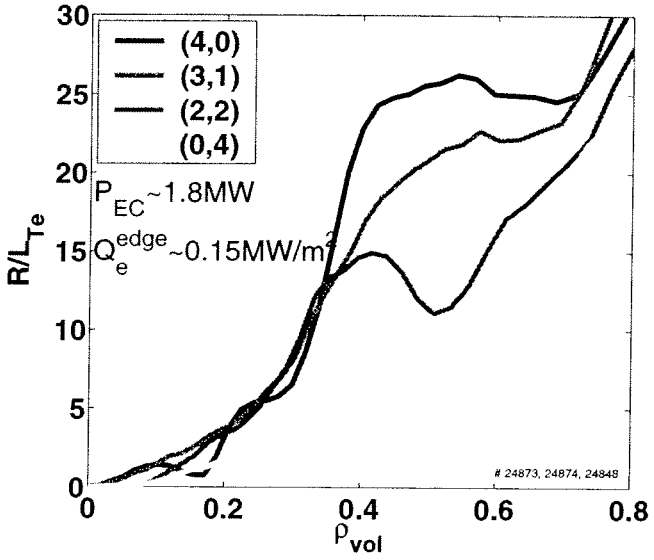

Figure 3b:

Normalised temperature gradient length R/L_{Te} variation at constant total EC power (P_{EC}~1.8MW) for different distributions of the EC power.

R/L_{Te} varies by a factor 5 at constant edge heat flux Q_e^{edge}.

highest values of R/L_{T_e} are obtained when all the EC power is deposited centrally, at ρ_1, peaking the T_e profile, whereas the lowest values are obtained when all the EC power is deposited off-axis, at ρ_2, broadening the T_e profile.

Concerning T_i, two features have to be pointed out. Firstly, as shown in **Fig 4a**, T_i depends weakly on the EC power and the ratio T_e/T_i ranges from 2 to 5 at δ~0.2, following essentially the T_e variation. Electrons and ions are weakly coupled at these low densities. Secondly, **Fig 4b** shows that T_i is 1.5 times higher at δ~0.2 than at δ~0.4. This is only partly explained by the geo-

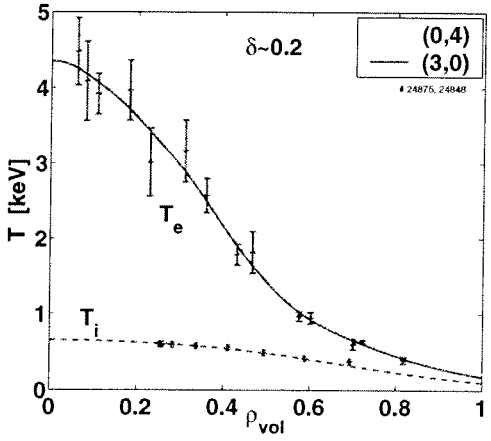

Figure 4a:

T_e and T_i profile for two extreme power deposition distribution at δ~0.2

T_e/T_i ranges from 2 to 5.

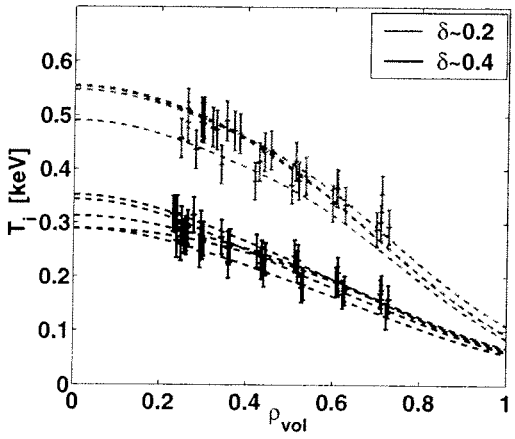

Figure 4b:

T_i profiles for δ~0.2 and δ~0.4

The whole T_i profile is lower at δ~0.4 than at δ~0.2.

metrical effect of flux surface compression which leads to larger regions with high ∇T_i values and hence lower confinement at high δ [5, 7]; the remaining variation could be due to the different Z_{eff} values observed at the two triangularities (Z_{eff} was typically 1.3 to 1.7 times higher at δ~0.2 than at δ~0.4).

4. Heat flux and temperature gradient length

The electron heat flux is evaluated through the following expression where all quantities are flux surface functions:

$$Q_e = \frac{1}{V'}\left\{\int_0^\rho P_{ohm}dV + \int_0^\rho P_{ECH}dV - \int_0^\rho P_{ei}dV - \frac{\partial}{\partial t}\int_0^\rho W_e dV\right\},$$

where V' is the derivative of the plasma volume with respect to the normalized radius. The ohmic power P_{ohm} is calculated assuming a radially uniform loop voltage. The ECH power deposition P_{ECH} is computed by the TORAY-GA linear ray tracing code [8]. The power transferred to the ions P_{ei} is evaluated using the ion temperature from CXRS and the electron temperature and density from Thomson scattering. The electron plasma energy W_e is calculated using the T_e and n_e profiles from Thomson scattering. Measurements from AXUV-bolometers (photodiodes) show that the radiated power P_{rad} never exceeds 20% of the total power P_{tot} and that for ρ<0.8, $P_{rad}/P_{tot} < 5\%$. P_{rad} is therefore negligible in the region ρ<0.8. In **Fig 5**, a power balance analysis for a typical shot in this set of experiments is shown. It is seen that P_{EC} strongly dominates the power balance, which validates the method as it allows for a strong variation of Q_e by changing only the EC power deposition distribution.

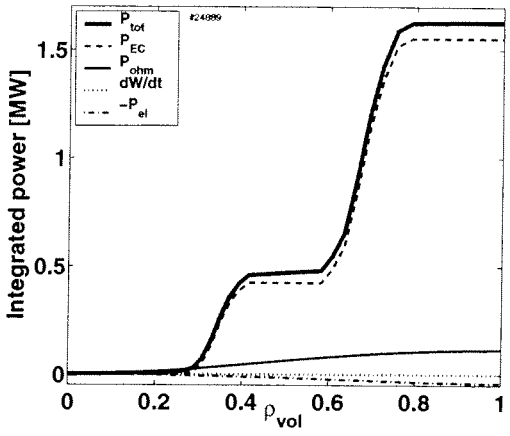

Figure 5:

Power balance analysis.

The various contributions are indicated, showing the dominant role of the EC power.

δ~0.4

At a fixed normalized radius, intermediate between the two EC power deposition radii ρ_1 and ρ_2, and for a given Q_e^{edge}, the local heat flux Q_e exhibits a threshold dependence in R/L_{Te} as shown in **Fig 6**. The threshold value for R/L_{Te} lies between 3 and 7, which is consistent with the

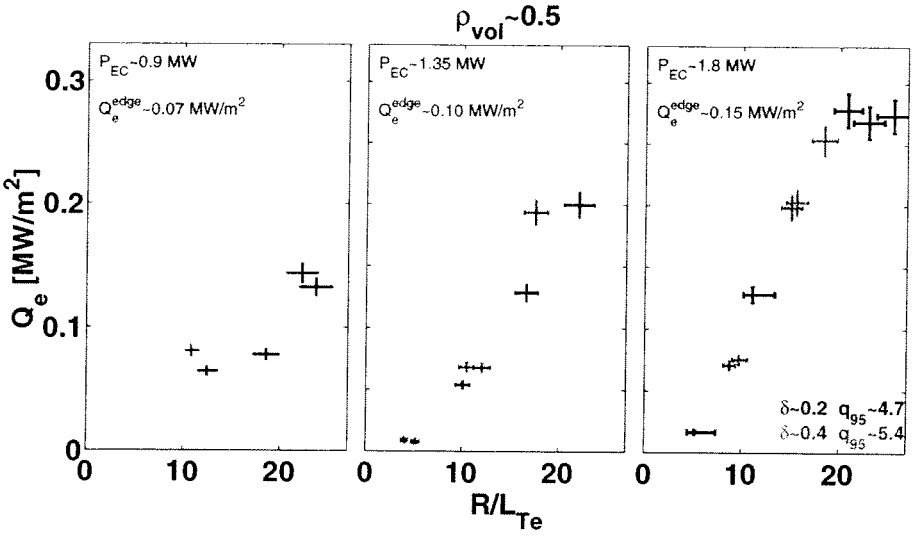

Figure 6:

Threshold behaviour of the heat flux Q_e variation as a function of R/L_{Te} for 3 values of Q_e^{edge} and at fixed normalized radius ρ~0.5.

values obtained in other tokamaks. It can also be noticed that the T_e profile becomes stiffer, i.e. $\frac{\partial Q}{\partial R/L_{Te}}$ increases, at high Q_e^{edge}.

5. Thermal diffusivity

The power balance analysis yields the electron thermal diffusivity through the relation:

$$\chi_e^{PB} = -\frac{Q_e}{n_e \nabla T_e}$$

With the power densities used in TCV, R/L_{Te} at mid-radius has been varied from 4 to 25, a range of values significantly broader than that explored in other tokamaks. **Fig 7** illustrates the corresponding range of χ_e obtained in TCV. For $R/L_{Te} < 15$, χ_e increases monotonically with R/L_{Te}, whereas it decreases for $R/L_{Te} > 15$. The behaviour is similar at all radii between the two power deposition locations, that is for $\rho_1 < \rho_{vol} < \rho_2$. The values of χ_e are comparable at both triangularities. The decrease of χ_e at high R/L_{Te} and for $Q_e^{edge} \sim 0.15 \mathrm{MW/m^2}$ occurs in the parameter region satisfying the Tresset criterion [9] for the formation of an electron internal transport barrier in TCV: $\rho_T^* = \rho_s / L_{T_e} > 0.06$, where ρ_s is the ion Larmor radius at the sound speed. It

should be noticed that the off-diagonal term involving the density gradient in the heat transport cannot explain the decrease of χ_e, as no correlation is found between these two parameters, even at a fixed R/L_{T_e}. The decrease of χ_e with R/L_{T_e} is more likely linked to a decrease of the micro-

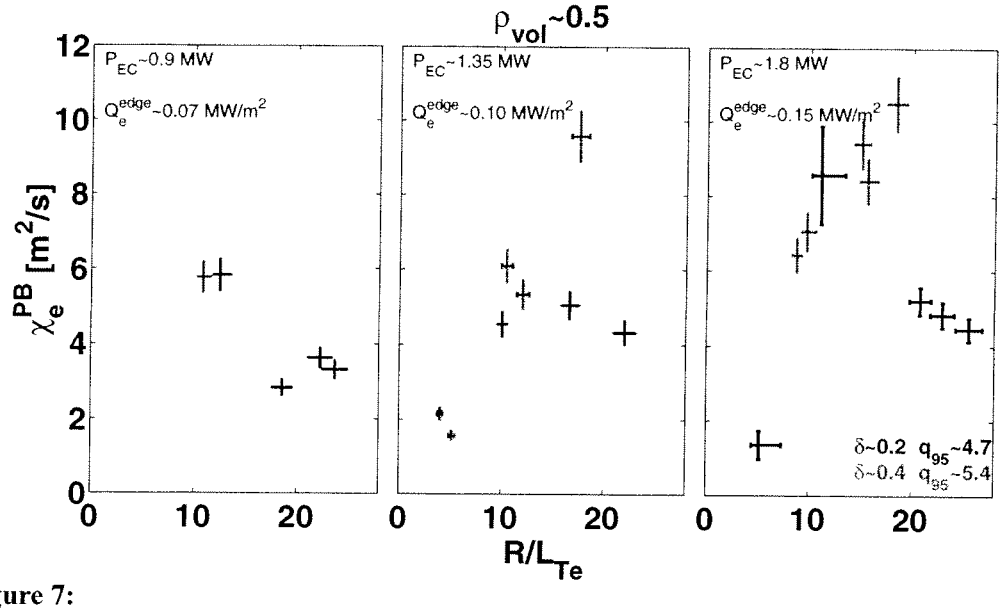

Figure 7:

χ_e at ρ_{vol}~0.5, from power balance analysis, as a function of R/L_{T_e} for 3 values of Q_e^{edge} and two triangularities.

turbulence with R/L_{T_e} or a correlated parameter.

Electron microinstabilities likely to be at play in TCV are electron temperature gradient (ETG) modes and trapped electron modes (TEM). At mid-radius, the experimental value of R/L_{T_e} is below the ETG threshold [10] for all the points shown in **Fig 7**. By contrast, while the experimental value of R/L_{T_e} is below the TEM threshold [11] for the three points with the lowest values of χ_e and $R/L_{T_e} < 7$, it exceeds the threshold for all the other points, consistent with the increased χ_e. In TCV, TEM are thus more likely to be responsible for the anomalous radial electron heat transport than ETG.

An analytical model with a threshold in R/L_{T_e} has been used in ASDEX Upgrade and JET to describe the experimental variation of χ_e [3, 4], according to the following expression:

$$\chi_e = q \cdot \frac{T_e}{eB} \cdot \frac{\rho_s}{R} \cdot \chi_0 + q \cdot \frac{T_e}{eB} \cdot \frac{\rho_s}{R} \cdot \chi_s(R\nabla T_e/T_e - \kappa_c) \cdot H(R\nabla T_e/T_e - \kappa_c)$$

In this expression, H is the Heavyside function. Below the threshold, χ_e is constant and characterised by the parameter χ_0, whereas above the threshold it increases linearly with R/L_{T_e}. A gyro-

Bohm scaling of micro-turbulence driven transport is introduced by the term $\rho_s \cdot T_e/(eB)$, where $\rho_s = \sqrt{2m_i T_e}/eB$ is the ion Larmor radius at the sound speed. The safety factor q compensates the decrease of χ_e towards the edge, due to the $T_e^{3/2}$ factor introduced by the gyro-Bohm term, and helps also keeping χ_s constant at different currents. This expression has allowed an adequate modelling of ASDEX Upgrade and JET data for R/L_{Te} between 2 and 10 [2, 12].

To test this model, χ_e normalized to $q \cdot T_e^{3/2}/(RB^2)$ is plotted in **Fig 8** for δ~0.2. As the model introduces a dependence on T_e, results for the three different Q_e^{edge} values are plotted on the same graph. For comparison, ASDEX Upgrade data from the experiments described in reference [1] are shown as well: the plasma shape and safety factor are similar (κ~1.6, δ~0.25, q_{95}~4.5) but, in ASDEX Upgrade, the heat flux is lower ($Q_e^{edge} \sim 0.04 \mathrm{MW/m^2}$) and the plasma is in divertor configuration. For $R/L_{Te} < 15$, the behaviour of $RB^2\chi_e^{PB}/(qT_e^{3/2})$ is qualitatively consistent with the model. The slope of $RB^2\chi_e^{PB}/(qT_e^{3/2}) = f(R/L_{T_e})$ is however lower in TCV than in ASDEX Upgrade. No statement can be made on the validity of the $T_e^{3/2}$ normalisation owing to the lack of points with different T_e and same R/L_{T_e}. For $R/L_{T_e} > 15$, the model clearly breaks down completely for TCV. The result is similar for δ~0.4. If it assumed that anomalous transport is driven by the trapped electron mode (TEM), the decrease of $RB^2\chi_e^{PB}/(qT_e^{3/2})$ with R/L_{T_e} could arise from a dependence of the threshold (acting on κ_c) or growth rate (acting on χ_s) on R/L_{T_e} or a correlated parameter.

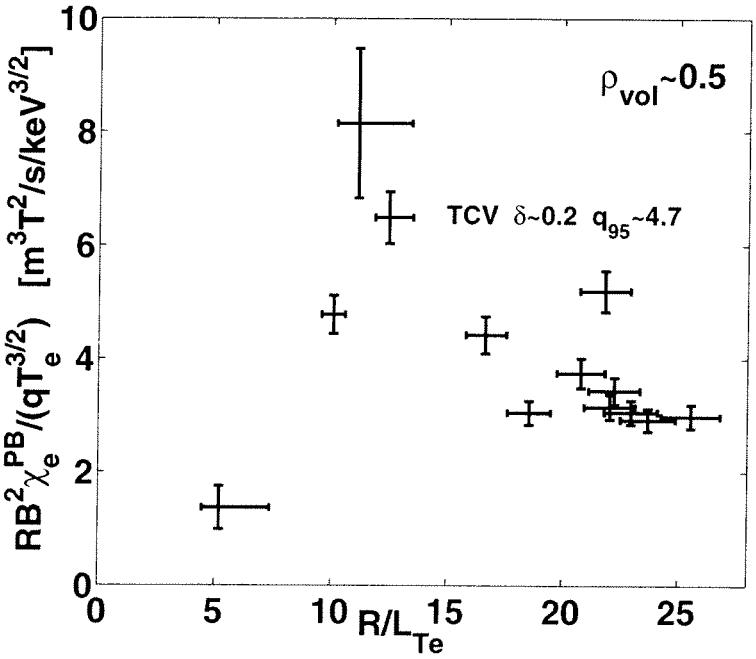

Figure 8:

Normalised χ_e as a function of R/L_{Te}

TCV and ASDEX Upgrade data.

6. Conclusions

The high ECRH power density in TCV has allowed a broad scan of ∇T_e and R/L_{T_e} at constant edge heat flux: R/L_{T_e} in particular has been varied from 5 to 25. For $R/L_{T_e} < 15$, the rela-

tion between χ_e and R/L_{T_e} is offset linear, as in other tokamaks. The slope, that is the stiffness, is found to be lower in TCV than in ASDEX Upgrade. A new and higher domain of R/L_{T_e} is explored in TCV, $15 < R/L_{T_e} < 25$, where χ_e stops increasing with R/L_{T_e}, which departs from the predictions of the model used in ASDEX Upgrade and JET, and which represents the domain of transition from stiff L-mode profiles to transport barrier profiles.

References

[1] RYTER, F., et al., Plasma Phys. Control. Fusion, **43** (2001) A323, and reference therein.
[2] RYTER, F., et al., Proc. 19th IAEA Fusion Energy Conference, Lyon, October 2002, CN-94/EX/C4-2Ra.
[3] IMBEAUX, F., et al., Plasma Phys. Control. Fusion **43** (2001) 1503.
[4] GARBET, X., private communication, 2002.
[5] BOSSHARD, P., Proc. 28th EPS Conf. on Plasma Phys. Control. Fusion, Madeira, 2001, P1.094,
BOSSHARD, P., Proc. 29th EPS Conf. on Plasma Phys. Control. Fusion, Montreux, 2002, P4.120.
[6] RYTER, F., et al., Phys. Rev. Lett. **86** (2001) 2325.
[7] MORET, J.-M., et al., Phys. Rev. Lett. **79** (1997) 2057.
[8] MATSUDA, K., IEEE Trans. Plasma Sci. **17** (1989) 6.
[9] TRESSET, G., et al., Nucl. Fusion **42** (2002) 520.
[10] JENKO, F., et al., Phys. Plasma **8** (2001) 4096.
[11] NORDMAN, H., et al., Nucl. Fusion **30** (1990) 983.
[12] MANTICA P., et al., Proc. 19th IAEA Fusion Energy Conference, Lyon, October 2002, CN-94/EX/P1-04.

Experience in Multibeam Alignment in TCV

T.P. Goodman and M.A. Henderson
1) Centre de Recherches en Physique des Plasmas, Association EURATOM - Confédération Suisse, Ecole Polytechnique Fédérale de Lausanne, CRPP - EPFL, CH-1015 Lausanne, Switzerland

e-mail contact of main author: timothy.goodman@epfl.ch

Abstract: The main aim of the upper launcher in ITER is the stabilization of Neoclassical Tearing Modes (NTMs). Efficient and effective stabilization requires generation of very localized driven currents, which in turn rely on localized absorption. As a general rule, it is necessary to ensure tight overlap of multiple independent beams. We discuss various aspects of aligning six beams on TCV using the response of the plasma to heating and current drive as the detector. Specifically, the EC deposition is routinely swept during shots and the sawtooth period is used to infer the beam size, power density and beam overlap from multiple beams. The physics of the sawtooth instability creates an ideal in situ detector of the relative power density and driven current when the plasma response is linear in power density: the "detector" appears to be smaller than the beam size. The method used for multi-beam alignment, which ensures high local power density as a result of tight beam overlap, will be described; from bench-top cold tests through laser alignment and plasma sawtooth period measurements. The impact on the design of the ITER upper launcher will be discussed.

1. Introduction

The stabilization, or reduction to an insignificant amplitude, of NTMs at the q=2 and q=3/2 surfaces has been demonstrated in the past [1,2,3]. NTM stabilization on ITER is the top priority for the upper launchers. Twenty megawatts are planned to be injected via three ports; each port having eight megawatts of installed gyrotron power transmitted via evacuated HE_{11} transmission lines to the launcher. The present ITER design is based on 1 MW gyrotron sources; however, Europe has undertaken the development of a 2MW source [4] to permit higher power per port or less stringent space requirements at the 20MW level, due to the reduced number of transmission lines required. In either option the total power from the 3 ports must be concentrated at the resonant surface of the modes in question to make efficient use of the available power. The width of the current channel driven by the beams must be smaller than the island width to make the island shrink and the width of the current channel will determine the ultimate minimum size of the island [5]. If the island can be driven below some minimum island width by the beams, other stabilizing effects can result in complete stabilization [6]. The smallest beam width occurs when all beams are concentrated at the exact same position. This paper will discuss the analogous problem encountered on the TCV tokamak when attempting to stabilize the sawtooth instability with multiple beams. It provides a record of successes and difficulties encountered during experiments designed to ensure accurate alignment of the 6 independent beams of the 2nd harmonic heating system.

The paper is organized as follows. Section 2 outlines the TCV electron cyclotron (EC) heating system [7] and the tests used to pre-align and calibrate the launching systems. Section 3 presents a short summary of previous results of sawtooth stabilization with both heating and current drive. This section also summarizes modeling of the experiments with the PRETOR-ST code. Section 4 compares and contrasts the TCV and ITER alignment situations and section 5 concludes with the suggestion of some steps that should be taken to ensure successful alignment of the upper launchers on ITER.

2. The TCV EC system and its initial alignment

TCV is equipped with nine, one-half megawatt gyrotrons. Six gyrotrons emit at 82.7GHz and three at 118GHz. The nominal pulse length is two seconds. The gyrotron output power is injected into an evacuated RF conditioning unit (RFCU, to use the ITER terminology) which, in the past, has been referred to more commonly as a "matching optics unit" or MOU. The RFCU contains focussing mirrors and grating-polarizer mirrors to prepare the beam for coupling to the 63.5mm evacuated HE11 transmission line and, further on, to the plasma itself. The 82.7GHz gyrotron beams are launched from the low field side (LFS) of the machine and the 118GHz beams from the top. The two frequencies are matched to the so-called 2nd and 3rd harmonic of the electron cyclotron frequency in the plasma and the polarization of each beam is generally adapted to couple to the X-mode of the plasma; although, the universal polarizer in the RFCU allows any polarization to be chosen. This leads to the nomenclature X2 and X3, used on TCV to designate the two frequencies.

At the tokamak, all three X3 beams are concentrated on one focussing mirror which can be displaced radially, between shots, and tilted in a poloidal plane, during a shot (FIG. 1). The beam trajectory in the plasma runs nearly parallel to the resonance surface, and the absorption profile is broad; providing bulk heating. The X3 launching system and its alignment will not be discussed further but, reference [8] provides some operational details.

The 6 X2 beams are all launched independently. The launchers are distributed non-uniformly in 4 of the 16 sectors of the torus. Four of the launchers are in upper ports and two in equatorial ports. The magnetic axis of the plasma in TCV tends to be located in the upper half of the vacuum chamber and thus, the equatorial launchers point upwards toward the plasma center while the upper launchers point downwards, in general (FIG. 2a). All launchers, however, can be oriented to provide toroidal injection for current drive (CD or ECCD) (FIG. 2b) as well.

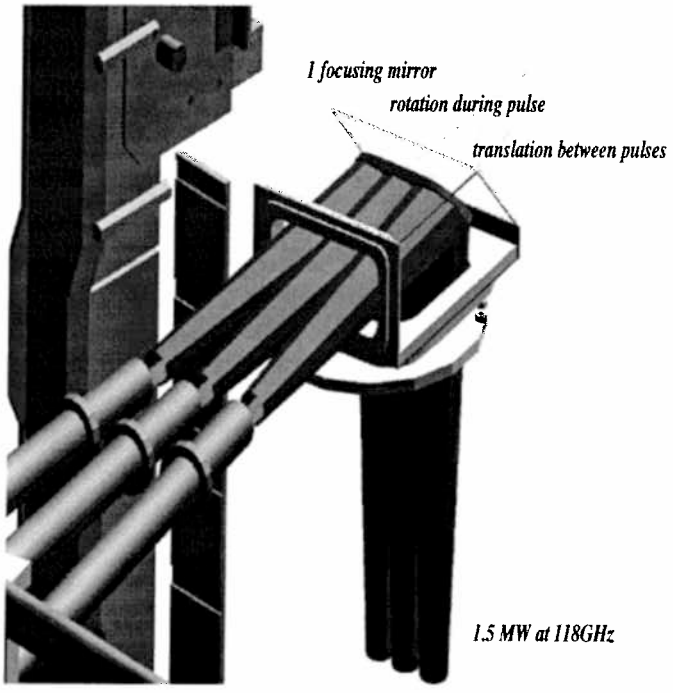

FIG. 1. The X3 launcher. One focussing mirror directs all three 0.5MW beams along the resonance surface in high elongation plasmas at densities higher than the X2 cutoff. The mirror can be rotated during a shot and displaced radial between shots.

The X2 launcher contains a 4 mirror assembly (FIG. 3). The last mirror of a launcher allows the beam to be swept in the plasma (96° /s) over a significant portion of the plasma minor radius; depending on the plasma elongation, resonance field location and beam refraction. The mirror movement is usually referred to as "poloidal" and is accomplished through vacuum bellows using short actuator rods which push on a drive plate. The drive plate houses a set of ceramic ball bearings which permits the mirror assembly to rotate providing toroidal injection; the toroidal motion being accomplished

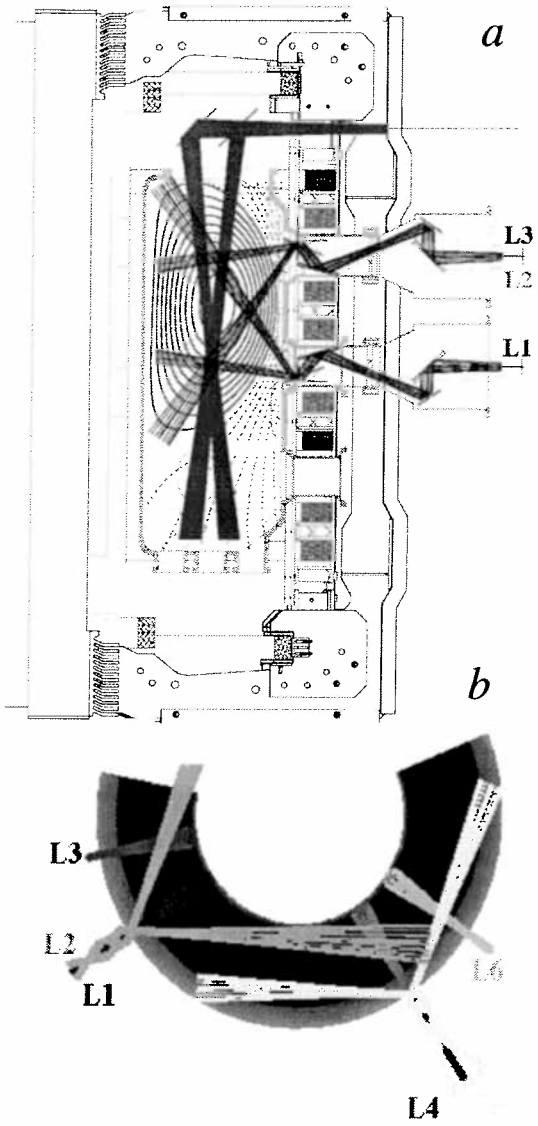

FIG. 2. a) Poloidal and b) toroidal cross-section of TCV showing the range of the launchers. Paraxial beam free-space trajectories are shown corresponding to the 1/e diameter in electric field. The X2 launchers can be rotated 360° for downward, upward, ±90° or intermediate aiming, as shown.

via a rotary vacuum feed through and a set of gears. Longer rods attached to this drive plate push on levers attached to the mirror which rotates about an axis. The return motion of the mirror is assured by 4 springs acting directly on the drive plate. Atmospheric pressure would cause compression of the springs when the launcher is evacuated. The springs are pre-compressed during installation to avoid deviation from the nominal rest position. The position is measured by linear potentiometers in the mirror control system. Once the launcher is assembled, it is cold-tested at its rest position using a low power HE_{11} input beam. Cross-sections of the beam are measured at several distances from the last mirror, along the theoretical beam axis, and fit to a 2-D Gaussian power profile. The center of the beam is thus traced and any errors in angle can be corrected by mechanical adjustments to the last mirror. The expected TEM_{00} waist propagation characteristics ($w(z)$) are also checked. This procedure allows correction of accumulated angle errors down to 0.06° on the launcher assembly (~1mm error in vertical height at the resonance). All significant errors in beam alignment have been eliminated by modifications to either the mechanical design of the mirror supports or assembly procedure. The low power measurement procedure can be eliminated without compromising the alignment when replaced by the appropriate mechanical tests

Once the launcher mirror assembly mechanical movement tests under vacuum have been carried out and the cold-tested in the laboratory have been completed, the mirror assembly is installed on the torus. Unlike the ITER launcher, the TCV mirror assembly could not be fixed directly to the port flange but is bolted, at the back end, to a removable vacuum chamber added to the torus chamber (see Figure 3); while the front end of the launcher is positioned by a frame attached directly to the torus chamber itself. During installation on the torus, the mirror assembly position is adjusted to insure smooth "toroidal" motion with the bolts tightened. Often the optimum position for smooth toroidal motion is slightly displaced from the theoretical position defined by the jig used to center the back end of the launcher..

Significant play in the actuator system results from the multi-stage assembly process. The play in the installed launcher is taken up by shims external to the vacuum that are individually

adjusted at the time of installation. Nevertheless, this complicated assembly procedure makes it absolutely necessary to check the launcher alignment once it has been placed on the torus.

The calibration of the actuator chain is carried out by a technician inside the torus once the launcher and the angle measuring electronics are installed. The angles of the fixed mirrors are checked with a digital level (0.1° sensitivity) to ensure that no relative misalignment between mirrors has occurred during installation; then, the measured angle given by the control electronics is calibrated against the digital level for ~5 angles. This calibration consists of a zero angle (intercept) and a slope, as the external cam of the drive system has been designed to provide a linear relation between the control voltage and mirror angle. Any error in the launcher axis, relative to the horizontal, should thus be taken into account by the calibration.

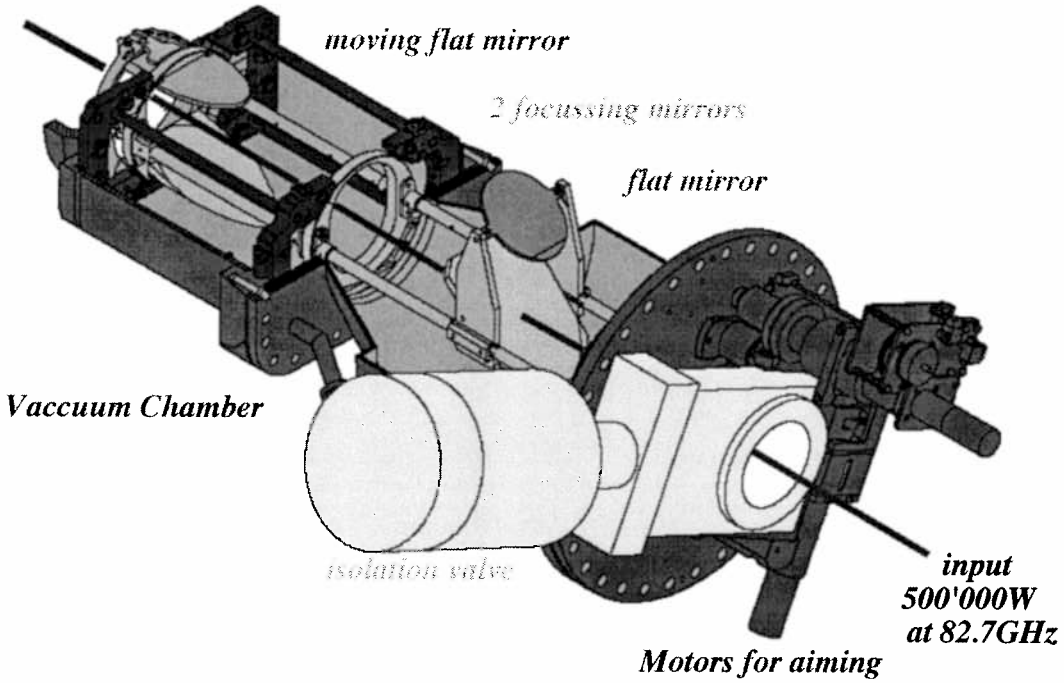

FIG. 3. The X2 launcher. The bellows, short actuator rods and drive plate are hidden behind the large green circular flange. The long actuator rods travel inside the cyan tubes to pivot the gray mirror at the TCV end. The dark blue frame is fixed to the TCV vacuum chamber and supports the 4-mirror launcher assembly (cyan + mirrors) at the TCV end by 3 ceramic bushings and 1 spring-loaded metal contact bushing which grounds the system. The entire cyan structure can rotate up to 360° about the launcher axis (dark red line) between shots.

The final calibration step involves injecting a laser beam aligned to the waveguide axis at the entrance of the launcher. The waveguide axis is aligned to be horizontal to the same accuracy, 0.1°, using the digital level. Laser alignment tests were attempted with limited success. The surface finish required for microwave mirrors is significantly rougher than for optical surfaces so the laser spot was very diffuse and difficult to localize. (This problem could be eliminated by optically polishing a flat section in the very center of each mirror which is "invisible" to the microwaves. e.g. A 4mm diameter flat could be machined at the mirror centers while introducing < 2μm error in the surface shape; or, an equivalent sized plug could be inserted into the mirror from the back providing the flat alignment surface.)

High power alignment using the actual transmitted beam at 82.7GHz is perhaps more relevant. Any error in angle due to mode mixture at the waveguide cut will be included directly. This

procedure entails difficulties of its own as an appropriate reference target is required in the torus and both personnel and machine safety must be guaranteed. A liquid crystal target was affixed to a plastic insulating sheet with double-faced tape and this was glued to a metal plate which was subsequently mounted on the central column of the torus vacuum chamber using the threaded holes designed for the carbon tiles. Their position is precisely known in the torus reference frame. A several-millisecond, several-hundred-kilowatt pulse was fired at the target and a photograph of the liquid crystal sheet taken. The error in the position is then estimated at ~6mm after 617mm corresponding to an error 0.6°. The maximum error expected at this stage is <0.2°. The high power test clearly reveals an unexpected misalignment not detected in the previous alignment stages. Unfortunately, this type of high power alignment is not suitable after launcher repairs or maintenance as it requires entry into the torus and removal of several carbon tiles. Another option would be to install a permanent detection system for *the actual millimeter wave beam produced by the gyrotron/RFCU/transmission line/launcher system.* Such a system does not exist on TCV, so this experience points to the requirement for an *in situ* plasma alignment procedure.

If we assume that this undetected error arises from the input beam to the launcher, it would imply an error in the output angle of the waveguide and therefore a coupling loss at the waveguide free-space transition. The magnification of the launcher system is ~1. The divergence angle $\theta_{div} = (2/k/w_0)$ of the beam which couples best to the free-space TEM_{00} mode is ~3.2° and the coupling loss due to angular misalignment alone would thus correspond to $P_{loss} / P_{in} \approx (\theta/\theta_{div})^2$ ~3.5% at 82.7GHz. (As the mirrors are large - diameter 4 times the electric field spot size on the mirror - the diffracted power loss through the launcher might be expected to be considerably lower.) Multiple high-power calorimetric measurements of the gyrotron power have a standard deviation of ±2%.

In contrast to TCV, the ITER launcher is part of a plug-in unit attached to the vacuum flange of the port and otherwise entirely independent of the torus chamber. Only a 20mm gap is available around the front (blanket) end of the launcher. Combined with the roughly 6m length of the launcher this defines a maximum physical misalignment of ~0.2° if the launcher were to touch the blanket at the front-end. As this will certainly not be permitted, the maximum alignment can be estimated to be less than half this value. The ITER port is inclined at an angle which presumably constitutes the reference angle of the plug-in; so, any error in the port angle, relative to the ITER reference coordinate system, is added to that of the plug-in within the port.

The "highly oblique launching" angles of the upper launchers in ITER may range from $|\alpha|$ ~ 73° to 53° while the maximum angle of the X2 launchers in TCV is 55° and X3 launcher angle from 85° to 90°. Errors in launcher angle translate into errors in $\rho_{deposition}$. The angle α – measured between the normal to the resonance cylinder and the k-vector in the poloidal plane – provides a rough estimate of the importance of this effect, in the absence of strong refraction. When heating near the top of a given flux surface the sensitivity to angle errors scales as $\Delta R/b/\cos^2(\alpha)$, where ΔR is the horizontal distance from the launch point to the resonance surface and b is the elongated minor radius ($\kappa = b/a$). A rough estimate of the typical situation for sawtooth stabilization discussed in this paper yields $\Delta R \sim 0.25$m, $|\alpha| \sim 20°$, $b \sim 1.4*0.25$m while for NTM stabilization in ITER $\Delta R \sim 0.75$, $|\alpha| \sim 63°$, $b \sim 1.7*2$m. Thus, despite the vast difference in size between the two machines, the sensitivity to angle errors is ITER is similar to that in TCV.

3. Summary of ECH and ECCD effects on TCV sawteeth

A strong dependence of the sawtooth period on the ECH deposition location in tokamaks has been demonstrated on many machines. For example, more than a decade ago, Hanada and co-workers [9] on WT-3 showed the asymmetry of stabilization (here meaning increase in the sawtooth period) between heating near q=1 on the high- and low-field-side of the magnetic axis, the non-linear increase in the sawtooth period when the power exceeded a certain threshold, the dependence of the power threshold on density and on q_{edge}, and finally that the ability to fully stabilize sawteeth required a small beam spot size (e.g. higher power density and/or better localization). Further, it was shown that the sawtooth period was very sensitive to the toroidal magnetic field; that is, the half-width of the region over which stabilization occurred for HFS heating was roughly the same size as the beam half width. It was suggested that modification of the local shear due to a heating-induced change in resistivity and therefore current density, was responsible for the observed sawtooth stabilization.

Experimental studies of ECH on the sawtooth period have been carried out on TCV since the first injection of power into the tokamak in 1996. The ECH deposition location ρ_{dep} was varied relative to the $q=1$ surface by either shot-to-shot radial scans, as on WT-3, or by single shot sweeps. Because of the flexibility of the TCV control system, its highly elongated vacuum vessel (3:1) and the equally flexible launchers, both radial and vertical sweeps are possible. Radial sweeps by variation of B_ϕ are used commonly on all tokamaks. (On TCV the maximum magnetic field limits deposition to essentially the HFS of the plasma axis.) In the vertical direction, however, the plasma is swept relative to the beam (z-sweep) or the beam relative to the plasma (θ - sweep) and heating occurs at a plasma poloidal angle of roughly $\pm 90°$ (top or bottom) rather than 0° (LFS) or 180° (HFS). In this case the deposition half-width $\delta\rho_{dep}$ is dominated by the projection of the Gaussian beam cross-section onto a resonance surface which is now roughly perpendicular to the flux surfaces rather than tangent (as in the B_ϕ sweeps) to them. The poloidal field creates an up-down asymmetry due to ECCD when aiming in the poloidal plane and during ECCD, trapped-particle effects can become important at the resonance location. All three of these differences can play an important role in determining the sawtooth period.

In parallel, theoretical studies and modelling of the sawteeth have been carried out since 1998 [10] using the PRETOR 1-1/2 transport code linked to a sawtooth model [11]. The resulting code is referred to as PRETOR-ST to designate the inclusion of the sawtooth model [12]. The sawtooth modeling is based on determining the moment at which the sawtooth crash occurs; that is, evolving the temperature and current profiles from just after a crash to the moment when a trigger condition is met. The trigger condition in TCV can be written as $s_1 > s_{1crit}$, where s refers to the shear and the subscript indicates evaluation at the $q=1$ radius. While both the shear and the critical shear (threshold value) evolve after a crash, in most cases, it is essentially the growth rate of s_1 which determines the sawtooth period: the slower the rise in shear at $q=1$, the longer the sawtooth period. Continued refinement of the modelling has allowed all of the experimental observations [13,14] using ECH and ECCD to be confirmed and has culminated in simulations and predictions related to sawtooth period *control* using both ECH and ECCD (or any electron heating and current drive system) [12].

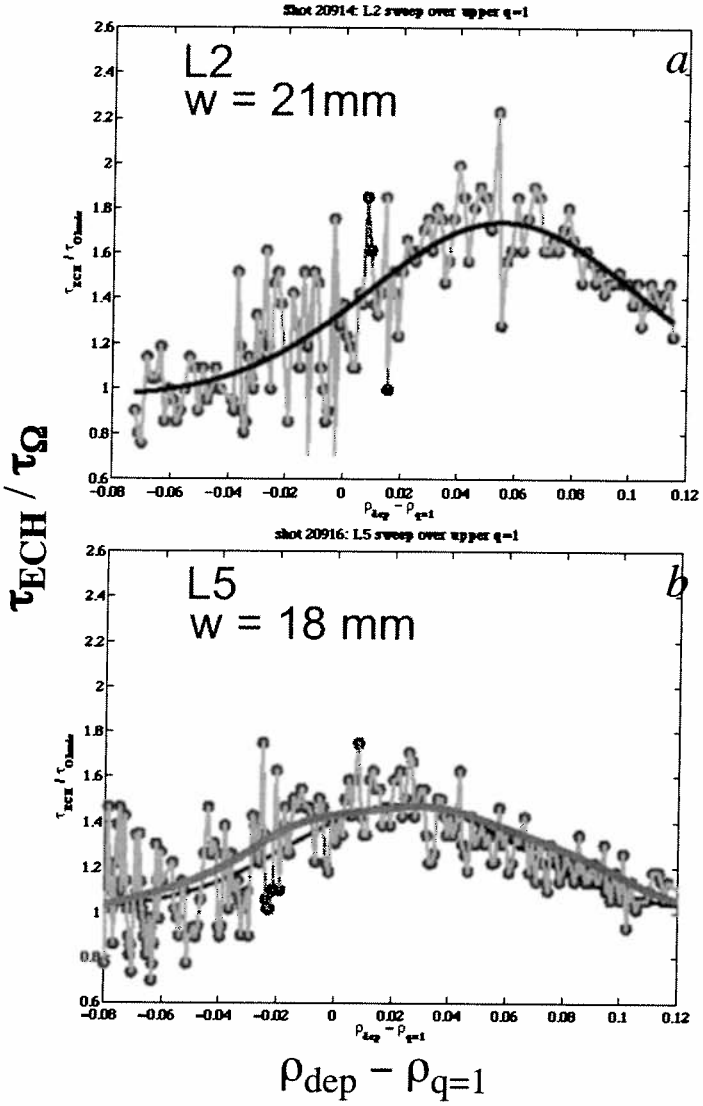

FIG. 4. Normalized sawtooth period versus ECH deposition location relative to q=1. The blue lines are Gaussian fits to the data. The 1/e power half-widths are ~20mm – similar to that expected for free-space propagation. The thick magenta curve in the b) is the ECH power density (0 offset to 1 on the graph) calculated by the TORAY-GA ray-tracing code at the Thomson measurement time closest to the peak in sawtooth period The offset between the beams is 0.026 which here corresponds to ~8mm or 1.3°.

Of particular importance to the discussion at hand, it has been shown that the sawtooth period evolution as a function of ρ_{dep} can indeed be used to measure the width and location of a single beam when swept in the plasma, as suggested in [13]. As an example, Figure 4 shows the sawtooth period (normalized to the no-ECH sawtooth period) as a function of ρ_{dep} - $\rho_{q=1}$ for two shots in which different launchers were swept. The deposition location can be defined by the maximum of the power density, or the location at which 1/2 of the beam power is absorbed. In most cases, the two coincide to within 0.01. When the deposition moves across the q=1 region, the q=1 radius moves. The deposition relative to the q=1 radius is used to eliminate, as much as possible, the effect this has on the fit parameters discussed below. When comparing sweeps, all beams are swept in the same direction (from inside to outside q=1) to avoid residual hysteresis effects [15] from this motion. TCV does not have a measurement of the poloidal field and therefore the motion is inferred from the motion of the inversion radius in some shots. The q=1 location given by the inverse equilibrium code LIUQE has been shown to be correlated to the inversion radius motion and, being more readily available, is more commonly used as the reference for the q=1 location. For this reason, the absolute value of the offset (e.g. +0.04) is not necessarily significant. In PRETOR-ST, the q=1 surface is calculated self-consistently with the current profiles and the relative position of the deposition to the q=1 surface is significant. PRETOR-ST clearly indicates that the optimum location for stabilization is the order of one beam half-width outside the q=1 location. As the same sawtooth trigger model will be incorporated in the suite of transport codes at DIII-D and similar sawtooth period measurements are now under way, this may soon be corroborated with MSE measurements.

Superimposed on the sawtooth periods measurements in Figures 4 are Gaussian fits to the sawtooth envelope. From these fits, the baseline (~1), amplitude, location and beam widths are found. Launcher 2 and 5 are seen to be offset in the location of their maxima by $\Delta\rho \approx 0.026$ which corresponds to ~8mm or 1.3°. Analysis of identical plasma shots shows reproducibilities ±10% in spot size, ±3% in amplitude and ±0.004 in location (±0.2° in angle). In Fig. 4b, the power density calculated by the TORAY-GA ray-tracing code is also shown. The maximum power density is ~2.5MW/m^3 at a local density of 2×10^{19}m^{-3}. The deposition profiles are calculated for the times at which the THOMSON scattering n_e and T_e profiles are measured. The profile shown is for the plasma and launcher parameters at the time of the measurement nearest to the peak in sawtooth period. The maximum timing error incurred is 25ms for a sweep of 1s (i.e. 2.5% of the full horizontal scale $\Delta\rho \approx 0.005$).

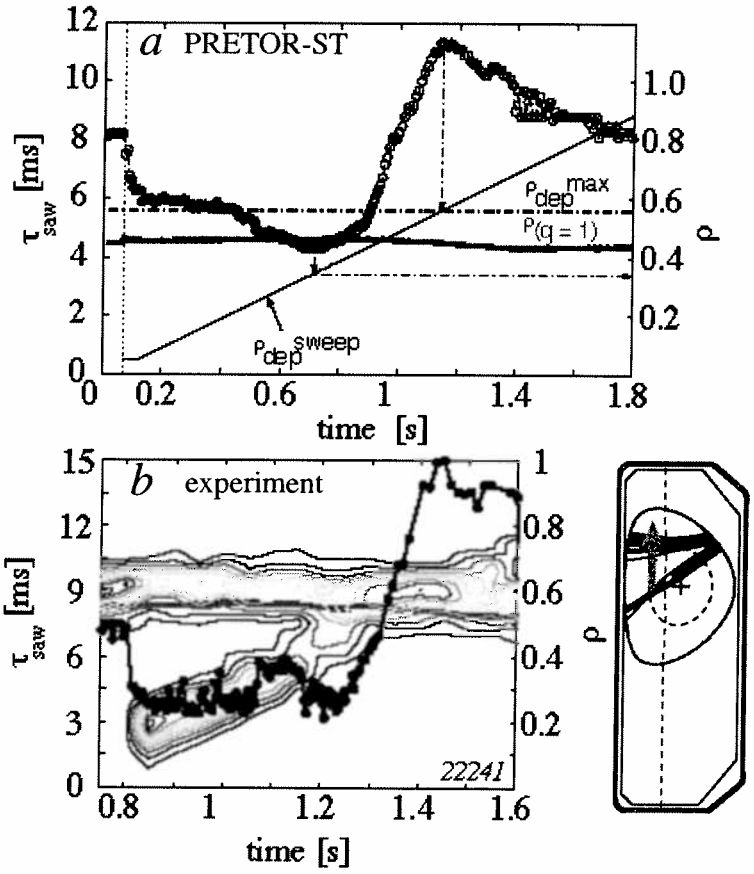

FIG. 5. a) PRETOR-ST sawtooth period predictions for 1.35MW fixed at ρ_{dep}^{max} and 0.45MW swept in time (ρ_{dep}^{sweep}). b) Similar experiment with 0.9MW at a fixed angle corresponding to ρ_{dep}^{max} (i.e. peak sawtooth period location from an earlier sweep) and 0.45MW swept. The right hand axis is the normalized radius ρ in both plots. The q=1 location is shown as a function of time as are the deposition locations: in b) they are indicated by 10 equal power density contours. (The aspect ratio of the plots has been adjusted to visually provide the same slope for the swept beam.) The swept beam destabilizes over a broad region inside q=1. [12].

In contrast to the *single* beam sweeps discussed above, the simplistic idea that the *q=1* surface can be used as a detector to measure the complicated power density profiles that can arise from simultaneous injection of *multiple* misaligned beams is incorrect. The sawtooth response is not simply the sum of positive definite terms when multiple beams are swept. As an example, when 2 beams are used to stabilize sawteeth, by heating at the optimum location outside q=1, and another beam is swept across q=1 for alignment (see Figure 5), the swept beam is strongly destabilizing over a broad region when ρ_{dep} is inside q=1: the beam has a "negative" effect. It might be suggested that two beams be considered as the linear sum of Gaussians, with a negative coefficient inside and positive coefficient outside q=1. However, it is clear (see Figure 6a) that with both beams outside q=1, the sawtooth period does not show a linear response to the power and the peak location is not found at the maximum of the total power density but, rather at the location of the inner beam. Without good *a priori* detailed knowledge of the sawtooth response to

various EC profiles and the beam spot sizes, the utility of the multi-beam sawtooth alignment method – combining beams and deducing the positions from the sawtooth period – is lost. Simulations are too unwieldy to work backwards from the measured sawtooth response to determine the deposition locations.

Dispite this difficulty, relative alignment between launchers using single beam sweeps has been performed. An example of re-calibration by signle sweeeps is shown in figure 6b. Launcher 1 and 2 were initially misaligned by 1.6°. A correction to the feedforward calibration was made and each beam was again swept separately to re-check the correction. Finally both beams were swept together and the sawtooth response can be seen to be significantly improved over the linear combination of the L1 + L2 fits as well as the combination of the misaligned beams from L2 and L5 (figure 6a). In the latter case, however, caution must be used as the sawtooth response is clearly non-linear in the power density and it is known that L1 has slightly more power than L2 while L5 has less power than L2; accentuating the difference in the combined sweep curves of Fig.'s 6a and 6b.

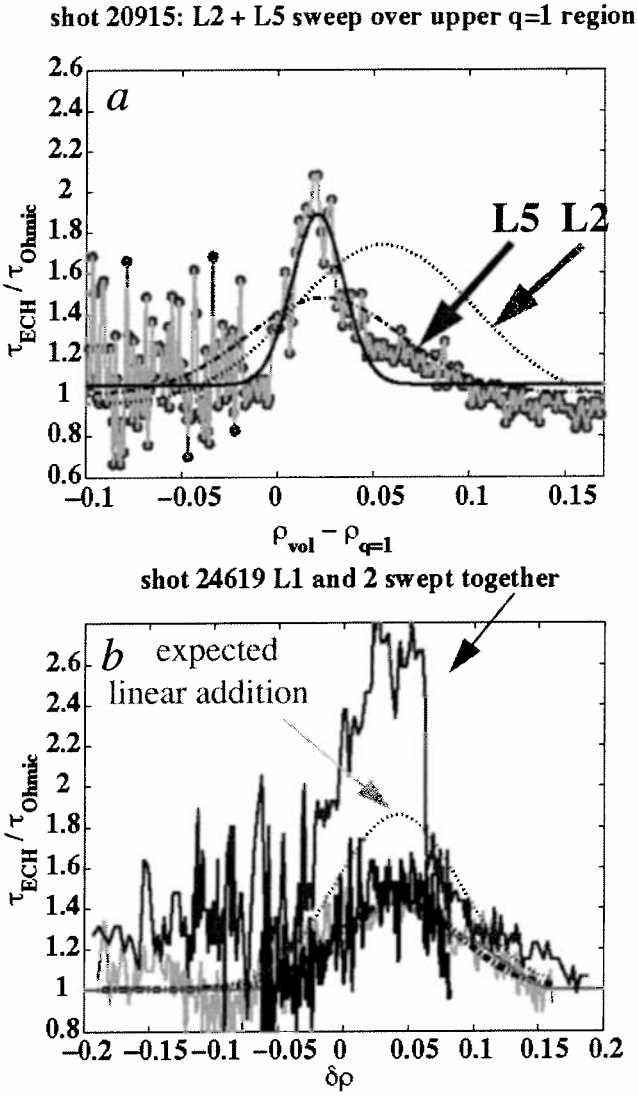

FIG. 6. a) Normalized sawtooth period versus ECH deposition location relative to q=1 when both L2 and L5 are swept at the same time. The dashed and dotted lines show the Gaussian fits from the single sweeps of figure 4. The solid blue line is a fit to shot 20915. The position is centered on the inner beam and the width is much narrower, as would be expected if the sawtooth response is non-linear in the power density. b) The same plot for L1 and L2 together in which good alignment is achieved. The sawtooth stabilization is much stronger.

For the small changes in sawtooth period measured in these plasmas during single beam sweeps, it is less clear that the amplitude and width of the peaks can be used to determine reliably the relative powers. For example, the Gaussian fits of figure 4 (shown also in figure 6a) suggest that L2 has at least 65% higher power than L5 (assuming that the beam half-widths are actually the same); a fact which is not borne out by power monitor measurements (corrected for the polarization) which indicate only ~33% more power in L2. Nevertheless, large differences in peak height are often indicative of some error in the optimization of the power coupling; e.g. bad polarization of the launched wave.

4. TCV and ITER alignment situations

The beams from the upper launcher in ITER will not reach the q=1 surface; so, sawtooth experiments cannot be used for alignment on ITER. Modulated ECCD experiments and localization with an ECE diagnostic will be possible in ITER: this diagnostic was not available on TCV when alignment was begun. What may be learned from the TCV experiments is that despite the best efforts made to insure proper alignment, multibeam stabilization of sawteeth did not proceed as expected. This difficulty was traced to relative misalignments of the beams. Testing of the beam alignment in the plasma is required.

Diagnoses of the multibeam problem was difficult even though the sawtooth instability in tokamaks has been thoroughly investigated for over a decade and models have existed for nearly half that time which can correctly simulate the observed sawtooth behavior. As an example, co- and counter- ECCD were not activated initially; although the possibility was present in the model, and it is only recently that a thorough investigation of ECH/ECCD effects has been carried out. This is understandable as the most relevant modeling studies (i.e. those that can be tested against existing data) are carried out first. A related issue is that models generally specify parameters of known or suspected importance to the physics; these are not always those which are controlled in an experiment. For example, ρ_{dep} may generally be held constant in PRETOR-ST while the launcher angle is constant in the experiments. Changes in the plasma profile which lead to differences in ρ_{dep} are therefore not simulated. This can, of course, be included *a priori*; however, the details included in the modelling are usually driven by the experimental results since their importance can be difficult to predict and time consuming to implement. Thus, PRETOR-ST had not been used to simulate the particular situation of misaligned beams and therefore could not provide guidance to the alignment experiments. For ITER it is desirable to change the methodology and use the construction period to simulate the worst case experimental scenarios with respect to alignment of beams for NTM stabilization. The modeling should be consistent with the real-time methods which are envisaged for beam alignment.

The normalized beam size in TCV for these investigations is ~20mm/1.4/240mm= 0.059. As an example, the current width over ±5° about the nominal angle in the ITER upper launcher ranges from 0.056 to 0.072 [16]. To benefit from higher power density stabilization in TCV, the estimated, required, beam overlap in TCV is ~ 1/2 the beam size (see Figure 6). Relative to the resonant surface ρ_s (for sawteeth $\rho_s = \rho_{q=1}$) a beam which is misaligned e.g. $\Delta\rho = \rho_{dep} - \rho_s$ by half the beam width can eliminate the stabilizing effects (see Figure 5a). A similar misalignment of the deposition location relative to the NTM resonant surface can also destabilize the NTM [17].

The point here is that the dimensions of interest in ρ on TCV and ITER are similar. Resolution of the misalignments on TCV is possible, but difficult, as the diagnostic resolution and knowledge of the equilibrium is of the order of the errors in alignment. The instability response to the heating, itself provides the required resolution due to its sensitivity to local parameters at the resonant surface: the location of the beam which is being aligned directly affects these parameters. In fact, if this were not the case, the misalignment would be inconsequential and thus irrelevant.

5. Conclusions

The experience of multibeam alignment on TCV urges caution regarding alignment in ITER. First, it should be assumed that the beams will be misaligned rather than the contrary. Even the best pre-alignment must be checked in the plasma. Second, both experiments and modeling should be done in present day machines with multiple (intentionally) misaligned beams to ensure that the NTM's respond as expected. Multi-beam NTM stabilization experiments heating near the top of the resonant surface are needed. Refining the models of stabilization and alignment algorithms will help minimize the required machine time on ITER. Finally, the feasibility of real-time, multibeam, feedback control should be carefully evaluated both by simulation and experiment.

This work was partly supported by the Swiss National Science Foundation.

6. References

[1] ZOHM, H., et al., Nuclear Fusion 39 (1999) 577.
[2] LA HAYE, R.J., et al., Phys. of Plasmas 9 (2002) 2051.
[3] ISAYAMA, A., et al., Plasma Phys. Control. Fusion 42 (2000) L37.
[4] PIOSCZYK, B. et al. this workshop.
[5] HEGNA, C. C. and CALLEN, J. D., Phys. of Plasmas 4 (1997) 2940.
[6] SAUTER, O. et al., Plasma Phys. Control. Fusion 44 (2002) 1999.
[7] GOODMAN, T.P., et al., in Proc. 19th SOFT, Lisbon, (1996) 565.
[8] ARNOUX, G., et al. this workshop.
[9] HANADA, K., et al., Phys. Rev. Lett. 66 (1991) 1974.
[10] SAUTER O., et al., Theory of Fusion Plasmas (Proc. Joint Varenna-Lausanne Int. Workshop) (Varenna 1998), ed. J.W. Connor, E. Sindoni and J. Vaclavik, ISPP-18 (Bologna, Editrice Compositori) (1999) 403.
[11] PORCELLI, F., et al., Plasma Phys. Control. Fusion 38 (1996) 2163.
[12] ANGIONI, et al., Nucl. Fusion 43 (2003) 455.
[13] GOODMAN, T. P., et al., Proc.of EPS Conf. on Contr. Fusion and Plasma Physics, Maastricht, 1999, ECA Vol. 23J (1999) 1101.
[14] HENDERSON, M.A., et al., Fusion Engineering and Design, 53 (2001) 241.
[15] GOODMAN, T.P., TCV Team, Proc. of IAEA-FEC, Sorento, 2000, [IAEA, Vienna (2001) EXP4/09].
[16] ITER Design Description Document, EC H&CD System, G 52 DDD 5 01-05-29 W 0.1
[17] POPOV, A. M., et al., Phys. of Plasmas 9 (2002) 4229.

A 2 MW, CW, 170 GHz COAXIAL CAVITY GYROTRON FOR ITER

B. Piosczyk[1], S. Alberti[2], A. Arnold[1,3], D. Bariou[4], A. Beunas[4], H. Budig[1], G. Dammertz[1], O. Dumbrajs[5], O. Drumm[1,3], D. Fasel[2], T. Goodman[2], M. Henderson[2], J.P. Hogge[2], S. Illy[1], J. Jin[1], C. Lievin[4], M. Thumm[1,3], M.Q. Tran[2], D. Wagner[6], I. Yovchev[2]

[1]*Forschungszentrum Karlsruhe (FZK), Association EURATOM-FZK, Institut für Hochleistungsimpuls- und Mikrowellentechnik, Postfach 3640, D-76021 Karlsruhe, Germany,*
[2]*Centre de Recherche en Physique des Plasmas (CRPP), Association Euratom-Confédération Suisse, EPFL Ecublens, CH-1015 Lausanne, Suisse*
[3]*Universität Karlsruhe, Institut für Höchstfrequenztechnik und Elektronik, Kaiserstr. 12, D-76128 Karlsruhe, Germany*
[4]*Thales Electron Devices (TED), 2 Rue de Latécoère, F-78141 Vélizy-Villacoublay, France*
[5] *Department of Engineering Physics and Mathematics, Helsinki University of Technology (HUT), Association EURATOM TEKES, FIN-02150 Espoo, Finland*
[6] *Max-Plank-Institüt für Plasmaphysik, Boltzmannstr.2, D-85748 Garching, Germany,*
e-mail: bernhard.piosczyk@ihm.fzk.de

Abstract

The development of an industrial prototype of a coaxial cavity gyrotron with an RF output power of 2 MW, CW at 170 GHz started recently in cooperation between European Associations (CRPP Lausanne, FZK Karlsruhe and HUT Helsinki) together with European tube industry (TED, Velizy, France). The engineering design is in progress. The fabrication of the prototype is foreseen to start in 2004 and the delivery of the prototype is expected for mid of 2005. The development work is based on results from detailed investigations performed on a 165 GHz coaxial cavity gyrotron at FZK in the last years. In parallel to the engineering design of the prototype the experimental coaxial gyrotron at FZK is under modification for operation at 170 GHz in order to verify the design of critical components in short pulse operation (~5-10 ms).

Introduction

To reduce the costs of the installations of the electron cyclotron wave (ECW) system at ITER and to allow a compact upper port launcher an increase of the output power per gyrotron unit is desirable. Coaxial cavity gyrotrons have the potential to generate a microwave power in excess of 1 MW in continuous wave (CW) operation at frequencies around 170 GHz since very high-order volume modes can be used. This is because the presence of the coaxial insert practically eliminates the restrictions of voltage depression and limiting current and in addition, the problem of mode competition is reduced by a selective influence of the diffractive quality factor of competing modes [1].

The feasibility of manufacturing a multi-megawatt coaxial gyrotron operated in CW has been studied during the last years at FZK Karlsruhe as an ITER task. The investigations have been performed on a coaxial gyrotron operated at 165 GHz in the $TE_{31,17}$ mode which is described in detail in [2,3]. The gyrotron is of modular type and enables an easy replacement of components. Its cooling performance allows only operation at short pulses (up to ~ 10 ms) with a low duty factor (~ 1/1000). Problems specific to the coaxial arrangement have been studied experimentally and theoretically and solutions have been demonstrated [2,3,4]. Among others the following investigations on the coaxial gyrotron and its components have been performed:

- coaxial insert: cooling requirement and losses, amplitude of mechanical vibrations under operating conditions, influence of radial misalignment on gyrotron operation, leakage current in dependence of the retarding collector voltage, demonstration of suppression of the build up of a Penning discharge inside the gun
- cavity and RF interaction: mode competition, range of single mode operation and efficiency of microwave generation, hysteresis effect and consequences on microwave power modulation [5]
- RF output system: conversion of the cavity mode into a free space Gaussian mode, microwave diffraction losses captured as stray radiation inside the tube body

Further on within the development work a new type of a coaxial magnetron injection gun (CMIG) with a cooled coaxial insert which is adjustable under operating conditions has been designed and tested [4]. The gun fulfils the main requirements for use in an industrial tube operated in CW. A design of a novel type of a high power collector capable to dissipate a beam power in excess of 2 MW, CW has been performed and the feasibility of manufacturing has been proven [6]. The requirements for the superconducting (SC) magnet have been specified. The suitability of all major gyrotron components for their use in a 2 MW, CW gyrotron has been examined and no principal technical constraints have been found. A first draft integral design of a 2 MW, CW coaxial gyrotron has been performed as shown in Fig.1. The overall dimensions of the gyrotron are comparable with the dimensions of a conventional gyrotron with an RF output power of 1 MW [7]. The obtained results demonstrate the basic feasibility for fabrication of a 2 MW, CW 170 GHz coaxial gyrotron and provide all data needed for a technical design and industrial manufacturing.

Based on these results the development of a coaxial cavity gyrotron with an RF output power of 2 MW, CW at 170 GHz as could be used for ITER started recently in cooperation between European Associations (CRPP Lausanne, FZK Karlsruhe and HUT Helsinki) together with European tube industry (Thalès ED, Vélizy, France). The engineering design of such a gyrotron is in progress. It includes a technical design and integration of all components as well as thermo-mechanical calculations and specifications of auxiliary systems needed for operation of the tube. The design phase will be finished end of 2003. The fabrication of the first prototype is foreseen to start

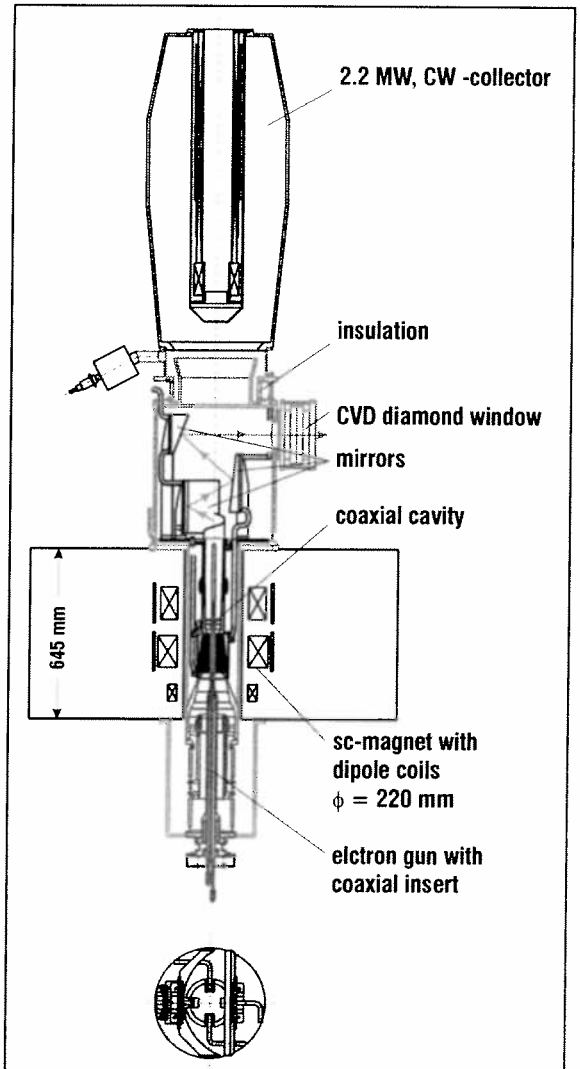

Fig. 1: Draft integral design of a 170 GHz, 2 MW,CW coaxial cavity gyrotron.

beginning of 2004 with a delivery of the prototype tube mid of 2005. In parallel a test facility suitable for testing the 2 MW coaxial gyrotron up to CW will be installed at CRPP Lausanne.

In order to test under realistic conditions critical components designed for the industrial prototype the experimental short pulse coaxial gyrotron at FZK operated at 165 GHz in the $TE_{31,17}$ mode is under modification for operation at 170 GHz in the $TE_{34,19}$ cavity mode. This modified coaxial gyrotron will be equipped with an electron gun which is very similar to the gun designed for the industrial prototype tube. The cavity and the quasi-optical RF output system will have the same geometry as designed for the prototype tube. Thus the generation of the high power electron beam, RF interaction and mode competition as well as the design of the RF output system will be verified and the amount of stray radiation will be measured under realistic conditions.

In the following, first the specification of the 2 MW coaxial gyrotron and the design of components are reported and some critical aspects are discussed. Finally the modifications on the experimental gyrotron are described.

2 MW, CW, 170 GHz Coaxial Cavity Gyrotron

Specifications and engineering design

The basic design of the 2 MW, CW coaxial cavity gyrotron and its components have been performed already. Constraints related to an operation at ITER have been taken into account. The main nominal design parameters are summarised in Table 1.

Table 1: Nominal operating parameters of the gyrotron and some design specifications

operating mode:	$TE_{34,19}$	
frequency, f	170	GHz
accelerating voltage, U_{acc}	90	kV
cathode voltage, U_{cath}	- 55	kV
body voltage, U_{body}	+35	kV
beam current, I_b	75	A
RF output power, P_{out}	2	MW
RF output efficiency, η_{out}	≥ 45	%
generated RF power, P_{RF}	≈ 2.2	MW
electron beam:		
average beam radius in the cavity, R_b	10.0	mm
velocity ratio, α	$\cong 1.3$	
SC magnet:		
magnetic field in the cavity, B_{cav}	6.86	T
diameter of the warm bore hole, Φ_{SC}	220	mm
cavity and coaxial insert:		
radius of outer wall, R_{cav}	29.55	mm
radius of coaxial insert at centre of cavity, R_{ins}	7.86	mm
Ohmic losses (twice the losses of ideal copper at 273 K; $P_{RF} = 2.2$ MW):		
peak losses at outer wall p_{cav}	2	kW/cm²
total losses at outer wall P_{cav}	54	kW
peak losses at coaxial insert p_{ins}	0.2	kW/cm²
total losses at coaxial insert p_{ins}	≈ 2	kW
collector (beam power to be dissipated):		
CW - operation	≤ 2.4	MW
operation with modulated RF power (0.6 - 2 MW):	≤ 3.1	MW

A CMIG gun [4] similar to the gun used in the short pulse experiments has been designed. At the nominal beam current the emitting current density is 4.4 A/cm^2. This value is compatible with requirements for the lifetime of at least 10000 h. The geometry of the technical part of the gun has been optimised to avoid trapping of electrons and thus the build up of a Penning discharge. According to the performed measurements the leakage electron current I_{ins} to the insert is expected to be below 0.1% of the beam current, $I_{ins} < 0.001 \times I_b$ at the nominal operating parameters. The total losses at the insert given in Table 1 contain both losses due to microwave absorption and dissipation due to the leakage current. In operation the accuracy of radial alignment of the coaxial insert relative to the electron beam has to be within $\Delta R_{ins} < \pm 0.15$ mm. In order to be able to fulfil the required accuracy the insert will be adjustable under operating conditions.

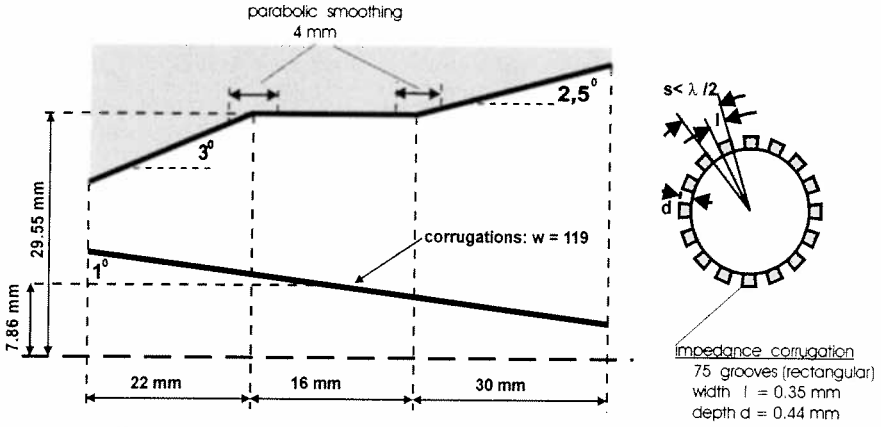

Fig. 2: Geometry of the $TE_{34,19}$ coaxial cavity

The $TE_{34,19}$ mode has been selected as operating cavity mode [8]. The geometry of the cavity is shown in Fig. 2. The design of the cavity has been verified by using two different time dependent, multimode and self consistent codes. With those codes the start up behaviour has been simulated considering up to 11 modes as competitors. The main mode competition was found to occur between the two mode triplets, $\{TE_{-33,19}, TE_{-34,19}, TE_{-35,19}\}$ and $\{TE_{+32,20}, TE_{+33,20}, TE_{+34,20}\}$. As an example the Figs. 3a,b show the start up scenario for three different values of the magnetic field calculated with a beam width (guiding centres) $\Delta R_b = 0$ mm (Fig. 3a) and $\Delta R_b = \pm 0.5$ mm (Fig. 3b) around the nominal beam radius $R_b = 10$ mm. The calculations have been performed for a beam voltage from 55 kV up to 93 kV. A dependence of the velocity ratio α according to the behaviour of a diode gun has been assumed with $\alpha = 1.3$ at a voltage of 90 kV and the beam current has been varied according to the Schottky effect with $I_b = 80$ A at 90 kV. The finite beam width has a small influence on the gyrotron oscillation, however, a wide range with single-mode oscillations can be obtained by a suitable selection of the operating parameters. The cavity will be made out of Glidcop. The Ohmic losses as well as the outer cavity wall and the insert (Tab.1) are within technically accepted limits. In thermo-mechanical calculations the maximum radial expansion of the cavity due to the Ohmic wall loading has been found to be 50 μm under stationary conditions which will be reached after about 0.4 s. The corresponding decrease of frequency is expected to be nearly 300 MHz. The deformation of the cavity causes a small increase of the Q-factor from about 1640 (cold) to 1700. Simulations of the start-up behaviour have shown that the influence of the deformation on the microwave generation can be compensated by reducing slightly the

magnetic field in the cavity. In order to demonstrate the feasibility of the cavity cooling a test of the cooling circuit will be performed.

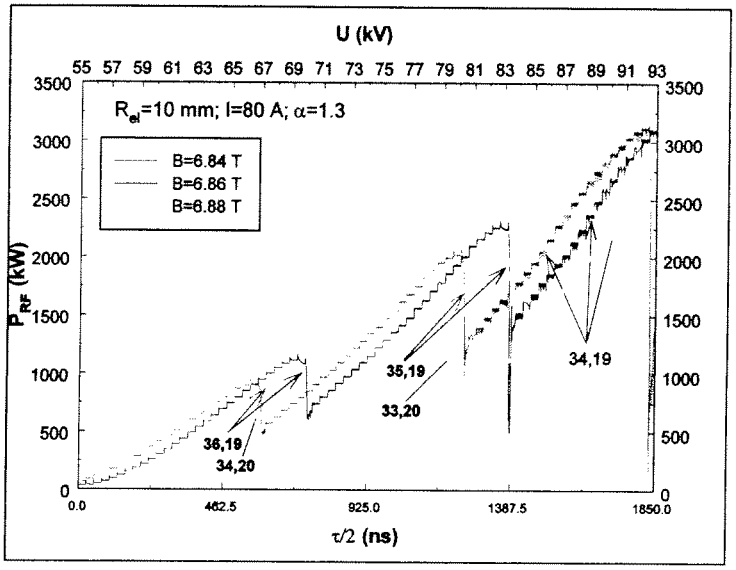

(- a -)

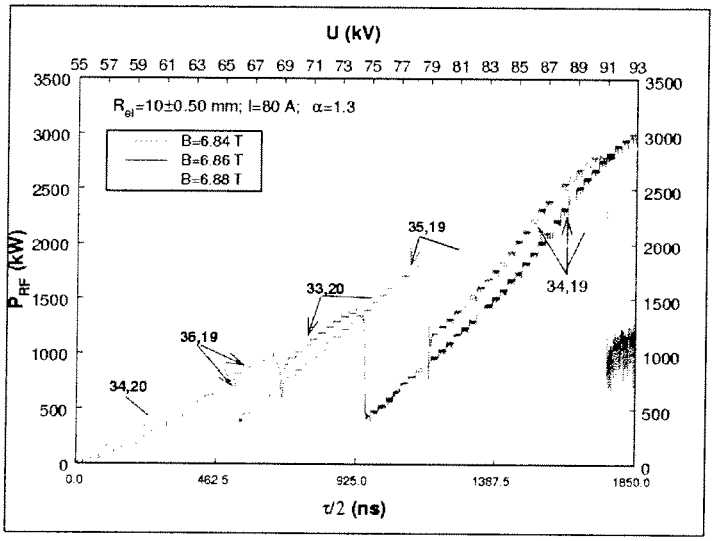

(- b -)

Fig. 3: Start up scenario in the $TE_{34,19}$ coaxial cavity. (a) $\Delta R_b = 0$, (b) $\Delta R_b = \pm 0.5$ mm.

The microwave stray radiation needs to be considered carefully since dissipation of the stray radiation power inside the gyrotron may result in an overheating of some parts which finally may limit the length of the pulses as observed in conventional 1 MW gyrotrons which are now under development for CW operation [7,9]. In the experimental 165 GHz gyrotron the total amount of microwave stray losses inside the gyrotron tube has been measured to be as high as about 9 % of the RF-output power. In this case the q.o. RF output system consisted of a simple smooth launcher with cut and of two mirrors. In order to reduce the diffraction

losses at the cut and thus to decrease the amount of microwave stray losses an improved q.o. RF output system has been designed. A rippled-wall launcher with reduced field amplitude at the edges of the cut similar as used successfully in the 140 GHz gyrotron for W7-X will be employed. In Fig. 4 the field distribution on the surface of the dimpled wall launcher is shown. The field pattern radiated from the launcher and the edges of the cut are marked. A schematic arrangement of the RF output system consisting of a launcher and three mirrors (one quasi-elliptical and two non-quadratic phase correcting mirrors) is shown in Fig. 5.

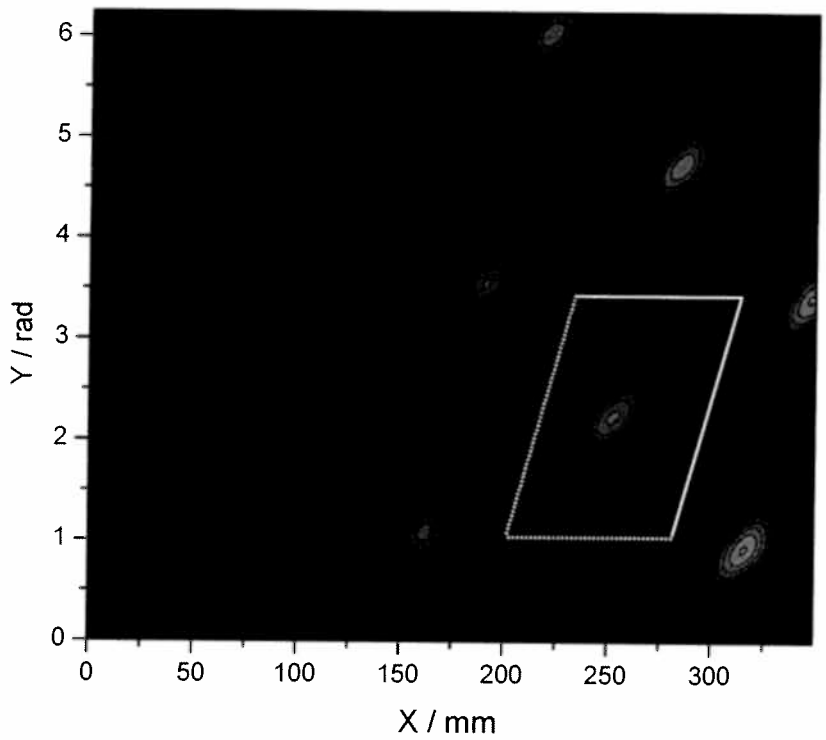

Fig. 4: Distribution of the H_z field at the surface of the launcher. The field distribution radiated from the cut and the edges of the cut are marked.

It is expected that with the improved RF output system the stray losses will be reduced in comparison to the values measured with a smooth launcher and that the losses can be reduced to 5 to 6 %. However, even at this value the corresponding microwave losses are around 100 kW. This requires an efficient reduction of the amplitude of the captured stray radiation in a controlled way either by well cooled microwave absorbing surfaces inside the mirror box and/or by efficient relief exits. Further on, in order to avoid an overheating of components due to dissipation of the stray microwave power the heat removal from all parts in particular the beam tunnel and all insulating ceramics have to be considered very carefully.

A single-disk CVD-diamond window with a thickness of 1.852 mm = $5\lambda/2$ at 170 GHz can be used for transmission of 2 MW microwave power at 170 GHz. At a loss tangent of 2×10^{-5} (state of the art) 880 W power will be absorbed in the disc. Edge cooling of the CVD diamond disc with water is sufficient for removing the heat load.

In order to fulfil the requirement concerning the microwave output efficiency a single-stage depressed collector with the collector at ground potential will be used. Under nominal operating conditions about 2.3 MW, CW beam power is remained and has to be dissipated in the collector. In operation with modulated microwave power (between about 0.6 MW and

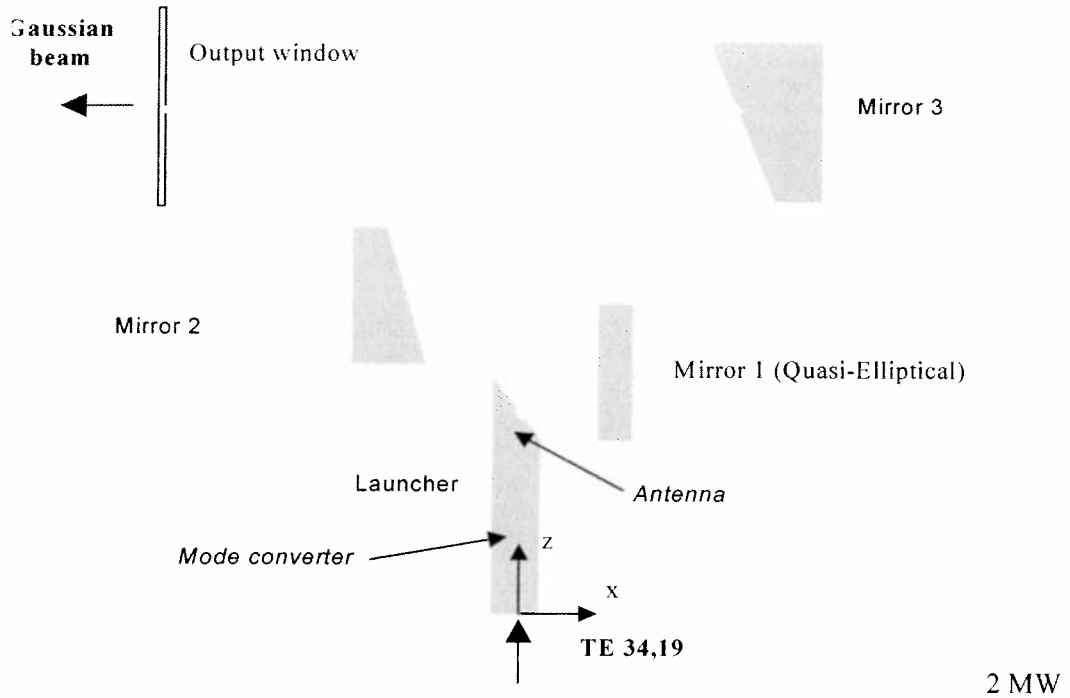

Fig. 5: Schematic arrangement of the RF output system

with 1:1 duty factor) the power dissipated at the collector rises to an average value of about 3 MW if as foreseen the power modulation will be performed by variation of the body voltage. A new collector with improved power distribution along the collector surface capable to dissipate 2.3 MW in CW operation has been designed as shown in Fig. 6. In order to be able to handle a power up to 3 MW, CW as would be needed for operation with modulated RF power a modification of the suggested design is under consideration with a maximum inner diameter up to 600 mm.

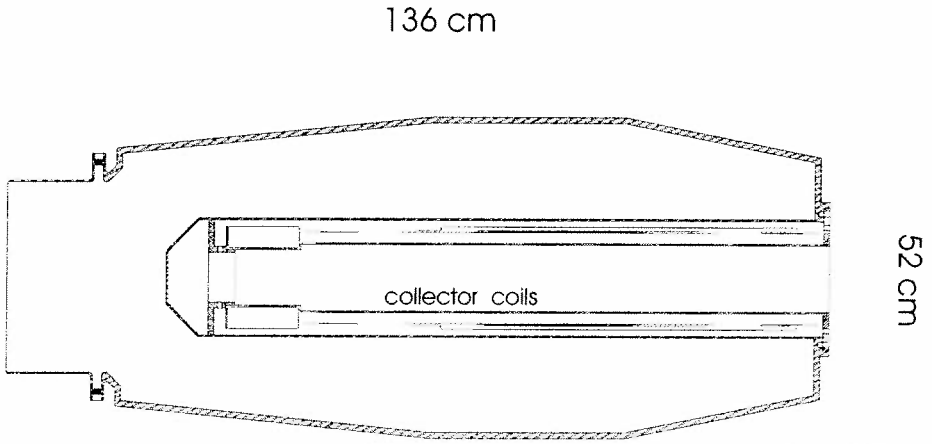

Fig. 6: Schematic view of the collector design for a dissipated power of 2.3 MW.

The requirements on the magnetic field distribution and the technical parameters of the SC magnet have been specified. The magnet will have a warm bore-hole with a diameter of 220 mm. The distance between the cathode position and the maximum of the magnetic field

has been defined to be about 380 mm. The magnet consists of a pair of main coils, a bucking coil and of two small gun coils which allow within certain range a flexible adjustment of the magnetic field in the gun region. In addition to the solenoid coils, the SC magnet will be equipped with a set of dipole coils, which are needed to perform the alignment of the coaxial insert under operating conditions.

Short-pulse experiments

In order to verify the design of critical components as electron gun, cavity and q.o. RF output system under similar conditions at short pulse (~ 5-10 ms) operation, the experimental 165 GHz coaxial gyrotron at FZK is under modification for operation at 170 GHz in the $TE_{34,19}$ mode. The maximum magnetic field of the used SC magnet of only 6.667 T requires a reduction of the operating voltage from 90 kV to 80 kV in order to be able to excite the nominal mode. The cavity and the quasi-optical RF output system will be identical as designed for the industrial tube. This will allow to prove the RF generation and mode competition as well as the efficiency of the RF output system and to measure the amount of the microwave stray radiation lost inside the tube under practically the same conditions. Numerical simulations of the RF interaction have shown that even at the lower beam energy an RF output power above 1.5 MW can be expected with the cavity as shown in Fig. 2. A new design of the electron gun (Fig. 7) very similar to the gun of the prototype, has been designed and is now under fabrication. Care has been taken to avoid regions with trapped electrons in order to suppress the build up of a Penning discharge which may limit the high-voltage performance. The modification of all components is in progress. Experimental operation of the experimental short-pulse gyrotron is expected to start beginning of 2004.

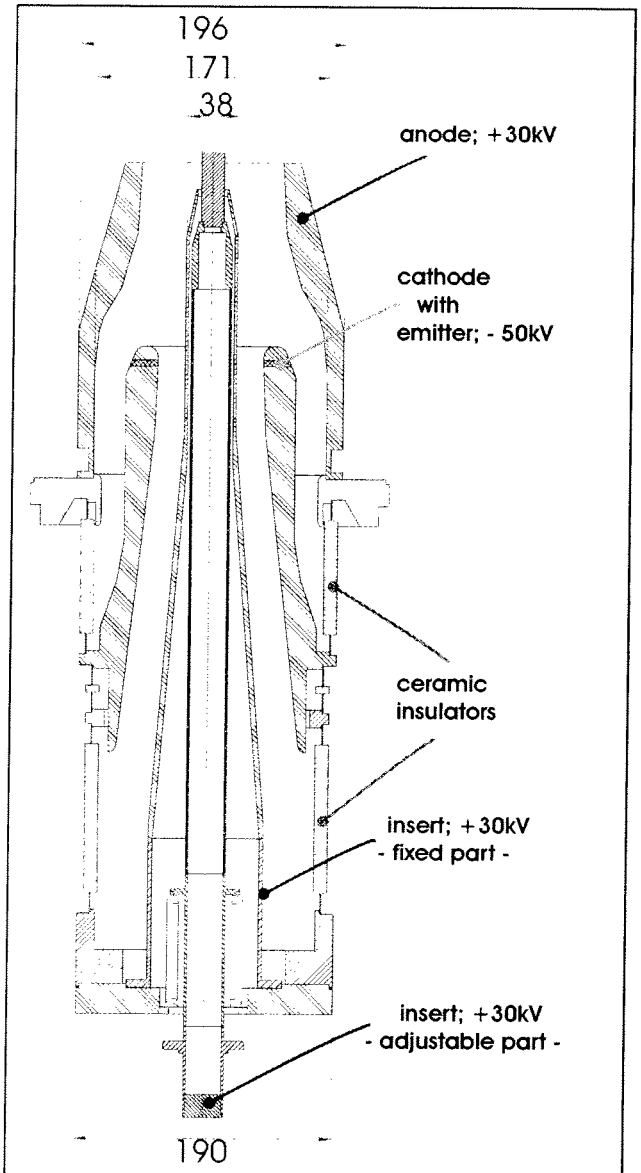

Fig. 7: Schematic arrangement of the coaxial magnetron injection gun for the experimental gyrotron. Dimensions in mm.

Summary and Outlook

The development of an industrial prototype of a 2 MW, CW coaxial cavity gyrotron at 170 GHz started in cooperation between European Euratom Associations (CRPP Lausanne, FZK Karlsruhe, HUT Helsinki) and European tube industry (Thales ED, Velizy, France). The final goal of the development work is to provide 2 MW, CW coaxial cavity gyrotrons for use at ITER. The engineering design is in progress and will be finished end of 2003. Thus the fabrication of a first prototype gyrotron is expected to start beginning of 2004. Then the gyrotron could be delivered mid of 2005. A suitable test facility is under preparation at CRPP Lausanne. The prototype will be considered as success if the specified parameters (Table 1) will be obtained for at least 1 s. The design of critical components of the prototype will be verified in short pulse operation with an experimental gyrotron which is now under modification.

Acknowledgments

The work was supported by the European Fusion Technology Program under the auspices of Program Nuclear Fusion of Forschungszentrum Karlsruhe and the Swiss National Science Foundation. The authors acknowledge the contribution of the gyrotron technical staff.

References

[1] C.T. Iatrou, S. Kern, A. Pavelyev *"Coaxial cavities with corrugated inner conductor for gyrotrons"*, IEEE Microwave Theory Tech. vol. 41, No. 1, pp56-64,1996.

[2] B. Piosczyk et al., *"Coaxial cavity gyrotrons - recent experimental results"*, IEEE Trans. Plasma Sci., vol. 30, No. 3, 819-827, 2002.

[3] B. Piosczyk et al., *"ITER ECRF advanced source development - coaxial cavity gyrotron final report"*, FZKA 6701, ISSN 0947-8620, Februar 2002, Forschungszentrum Karlsruhe.

[4] B. Piosczyk, *"A novel 4.5 MW electron gun for a coaxial gyrotron"*, IEEE Trans. Electron Devices, vol. 48,12, 2938-2944, 2001.

[5] O. Dumbrajs et al., *"Hysteresis-like effects in gyrotron oscillators"*, Physics of Plasmas, vol. 10, No. 5, pp. 1183-1186, 2003.

[6] B. Piosczyk , *"A 2.2 MW, CW collector for a coaxial cavity gyrotron"*, 26th Inter. Conf. on Infrared and Millimeter Waves, Toulouse, France, Sept. 10-14, 2001.

[7] G.Dammertz et al, *"Development of a 140 GHz, 1 MW, Continuous Wave Gyrotron for the W7-X Stellarator"*, IEEE Trans. Plasma Sci., vol. 30, No. 3, 808-818, 2002.

[8] O. Dumbrajs et al., *"Mode selection for a 2 MW, CW 170 GHz coaxial cavity gyrotron"*, 26th Inter. Conf. on Infrared and Millimeter Waves, Toulouse, France, Sept. 10-14, 2001

[9] K. Sakamoto et al., *"Development of gyrotron and JT-60 EC heating system for fusion reactor"*. 19th IAEA Fusion Energy Conf., CT-07Ra, Lyon, France, Oct. 14-19 2002.